Dependence of the transport in channel models of the ACC on the Rossby radius of deformation

by

Louis-Philippe Crevier

Department of Atmospheric and Oceanic Sciences
McGill University
Montreal

A thesis submitted to the
Faculty of Graduate Studies and Research
in partial fulfillment of the requirements for the degree of
Master of Science

ABSTRACT

It has been suggested that the transport of the Antarctic Circumpolar Current is set, essentially, by the southward Sverdrup flux at latitudes just north of Drake Passage. Although this idea is consistent with observations, it has been critized in that Sverdrup dynamics fail at Drake Passage latitudes. Here, we think of the total transport as being comprised of two components: one associated with the basin-like dynamics to the north of Drake Passage and the other associated with the dynamics of the Drake Passage latitude band itself. The Drake Passage latitudes are often simulated using channel models with bottom topography. For a two-layer channel, large topography effectively blocks geostrophic contours at depth and allows zonally-reconnecting contours in the upper layer. This concentrates the through-channel transport in the model's upper layer. Furthermore, it is argued that the statistical steady state for wind-driven channel flow (that is not too viscous) should be baroclinically unstable. Assuming marginal instability then leads to an estimate of the through-channel transport.

A two-layer primitive-equation channel model with bottom topography and wind forcing is used to test this relationship. Model integrations are made to obtain statistical steady states for a range of parameters. The Rossby radius and the wind strength are varied as the theory predicts that transport should go like the square of the former and be relatively insensitive to the latter. Integrations to test the robustness of these results to model resolution are also conducted.

RÉSUMÉ

Il a été suggéré que le transport du Courant Circumpolaire Antarctique était essentiellement déterminé par le flux Sverdrup provenant des latitudes au nord du Détroit de Drake. Bien que cette idée soit cohérente avec les observations, elle a été critiquée dû au fait que les dynamiques sverdrupiennes sont inapplicables aux latitudes du Détroit de Drake. Ici, nous traitons le transport total comme étant formé de deux composantes: l'une reliée aux dynamiques de basin au nord du Détroit de Drake et l'autre reliée aux dynamiques des latitudes du détroit lui-même. Les latitudes du Détroit de Drake sont souvent simulées à l'aide de modèles de canal incluant une topographie océanique. Pour un canal à deux couches, une topographie de grande taille bloque les contours géostrophiques au fond et permet l'apparition de contours circumpolaires dans la couche supérieure ce qui concentre le transport du canal dans cette couche. De plus, nous argumentons que l'équilibre statistique de l'écoulement (peu visqueux) dans un canal, forcé par le vent, devrait être barocliniquement instable. En supposant une instabilité marginale, nous pouvons ainsi obtenir une estimation du transport du canal.

Un modèle de canal à deux couches, aux équations primitives et comportant la topographie et le forçage du vent est utilisé pour tester notre estimation. Des simulations sont faites de façon à obtenir l'équilibre statistique pour un éventail de paramètres. Le rayon de Rossby et le vent sont variés puisque la théorie prédit que le transport devrait évoluer comme le carré du premier et être relativement indépendant du second. Des simulations pour tester la dépendance des résultats face à la résolution du modèle sont aussi complétées.

Contents

List of Figures

List of Tables

I first wish to thank my supervisor, David Straub, who greatly helped me throughout these last two years. His comments (especially during the preparation of this thesis) were always constructive and supportive. We may not have always chosen the fastest road the first time but we traveled on the most interesting one all the time.

Many thanks to Fred, Rob and Badri for helping me to get the model to finally work. Also thanks to Alex, Jason, Ravi and lots of others for those wonderful discussions about nothing and everything. They were a great way to deepen our understanding of science and to relax after (or during...) a very stressful day. And, of course, having a vast knowledge of the Simpsons and South Park is not a bad thing in itself!

Thank you Marie-Claude for your support and understanding. It wasn't easy being so far apart for so long. But now that we will be together, it will even be harder... to concentrate on my work!

Finally, many thanks to Mariel, Pierre, Jean-François, Caroline, all the Leclercs(!), Mamie, Papi (two times each) and all my friends for your support and encouragement.

Funding for this project was provided by the Centre for Climate and Global Change Research and by grants from NSERC and AES. The computing facilities of the Centre de Recherche en Calcul Appliqué (CERCA) and the Department of Atmospheric and Oceanic Sciences were used for this work.

Chapter 1

Introduction

The Southern Ocean constitutes a very distinct biological and hydrographic environment from the world's other major oceans. Extending from the coast of the Antarctic continent all the way out to the 50 degrees south parallel, it contains the world's farthest point from land near the middle of the South Pacific. Almost only accessible in the austral summer, this region has only begun to reveal its secrets a short while ago. The frigid antarctic atmospheric conditions along with the sea-ice formation produce the densest waters on Earth. Also, the nutrient-rich waters of the Southern Ocean support a great diversity of marine life that remains fairly isolated from the waters of the South Pacific, the Indian Ocean and the South Atlantic. This is quite particular, as there is no physical boundary separating the Southern Ocean from these other oceans. But, then again, the northernmost region of the Southern Ocean is particular in that it embeds one of the Earth's most important currents.

The Antarctic Circumpolar Current (ACC) is the only zonally reconnecting current on Earth. As its name implies, it circles the Antarctic continent at about 50 degrees south of latitude. Its flow forms a circle with a circumference of about 25,000 km, making it the longest current on Earth. The physical structure of the ACC flow

possesses some very unique properties that are closely related to the structure of the Southern Ocean itself. It also presents an interesting problem to modelers, as its dynamics are fairly different from those of the other major currents of the world's oceans.

1.1 Southern Ocean characteristics

The ACC is a wind driven ocean current (*e.g.*, Stommel, 1962). Westerlies are blowing across almost all of the Southern Ocean and these winds drive the eastward quasi-zonal flow. The ACC is a broad current, much larger than other wind-driven current which generally are about the same width as the internal Rossby radius of deformation in their vicinity. While the main part of the transport occurs in two jets that run almost parallel to the 50° south latitude circle, the current is as broad as Drake Passage, the region between the southern tip of South America and Antarctica, itself (Nowlin and Klinck, 1986). The jets follow the subpolar and polar fronts across which the water properties change sharply. We can see from figure 1.1 that the flow is essentially zonal and eastward except in the regions just east of New Zealand and South America. There is also a drift towards the south over all of the ACC path. The jet locations (on both boundaries of the ACC path in figure 1.1) evolve with time and the jets may meander hundreds of kilometers north or south of these locations. This structure is different from that of other wind driven currents which generally constitute only one broad flow. We can note that the two jets have different water characteristics but these remain almost uniform throughout each jet.

Another particularity of the ACC resides in the fact that the flow extends all the way to the bottom of the ocean. The year-averaged flow velocity varies with depth and has a characteristic maximum value of the order of 0.60 m s^{-1} at the surface and about 0.25 m s^{-1} at 3000-m depth. A small countercurrent (e.g westward) is expected

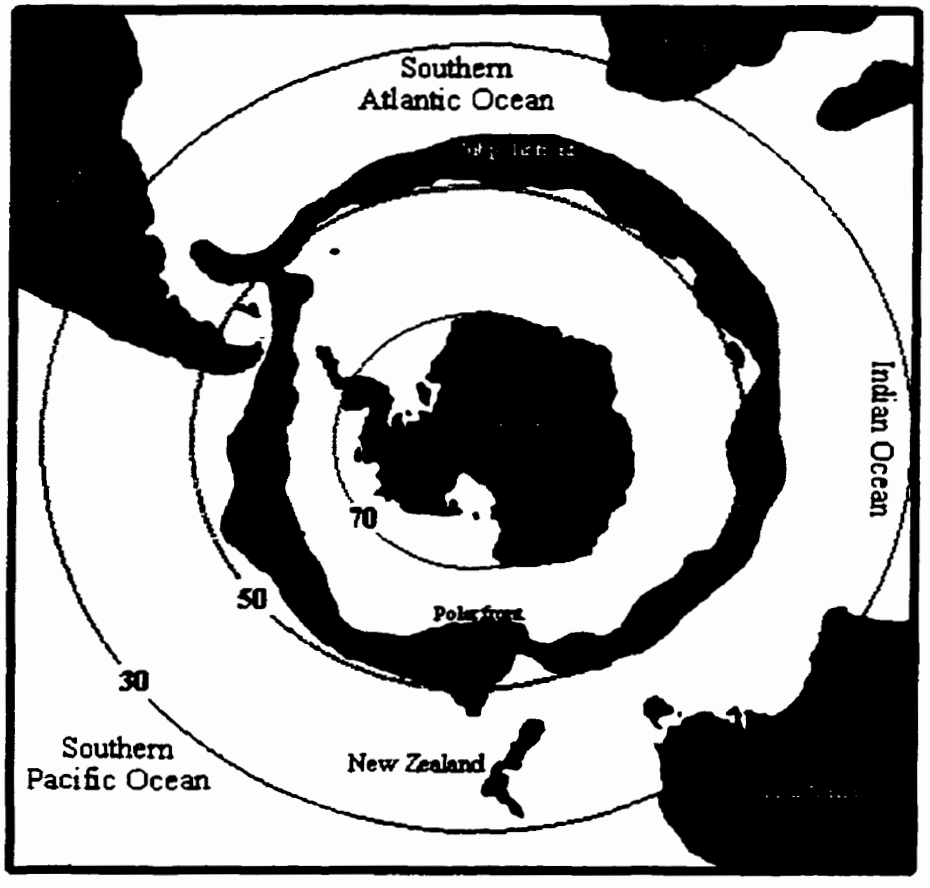

Figure 1.1: Sketch of Antarctic Circumpolar Current path. ACC is in gray and cycles clockwise. The two jets are located at the southern and northern boundaries of the ACC. Path is based on ACC jets displayed in figure 1 of Whitworth (1988).

to exist along the coast of Antarctica, near the bottom of Drake Passage (Olbers and Wenzel, 1989). These velocities are significantly smaller than those of other currents like the Gulf Stream (≈ 1 m s^{-1}). On the other hand, the transport is much larger as a significantly larger volume of water is moving along the same direction. The mean transport through Drake Passage is of the order of 130 Sv (1 Sv $= 10^6$ m^3 s^{-1}) (Whitworth *et al.*, 1982; Whitworth and Peterson, 1985). The transport thus displays a significant amount of variability (about 20%) and can undergo very rapid increases or decreases. Data from the late 1970's International Southern Ocean Studies (ISOS) study of the ACC at Drake Passage showed that the transport varies between 110

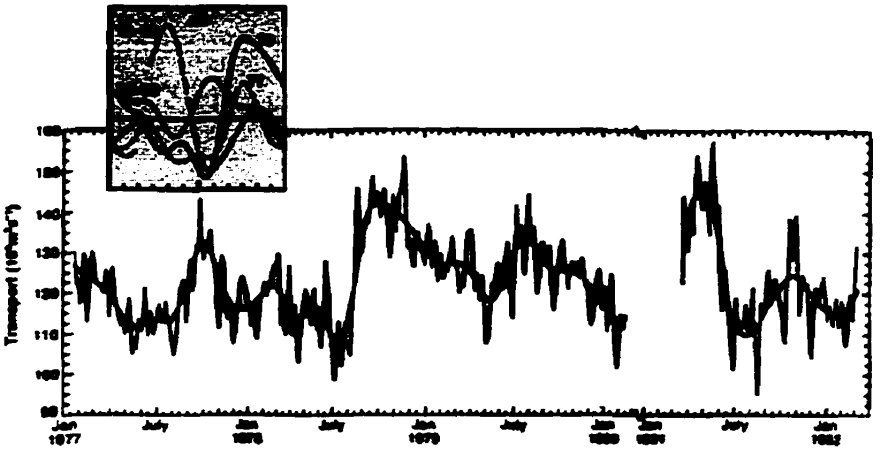

Figure 1.2: Transport time series for Drake Passage (from Whitworth and Peterson, 1985, figure 3). The light line shows fluctuations in transport at periods greater than 10 days. The heavy line is a smoothed version of the data to illustrate the longer term changes in transport. The inset shows the smoothed data as four 1-year segments and demonstrates that year-to-year differences in transport are larger than any seasonal similarities.

Sv and 145 Sv. The ISOS study was conducted over a four year period with three summer expeditions and one fall expedition being undertaken. Figure 1.2 shows the time series of transport through Drake Passage (from Whitworth, 1988). While the large-scale variability gives the impression of being a seasonal cycle, it varies strongly from year to year. Most of the transport variability is seen in the barotropic field. Transport fluctuations across Drake Passage are well correlated with the wind stress variations (Wearn and Baker, 1980). The transport lagged the wind stress by only 9 days and this quick adjustment implies barotropic transport fluctuations. Only long time scale changes in wind stress are therefore expected to cause changes in the Southern Ocean's baroclinic transport structure. Recent measurements by Meredith *et al.*(1996) tend to confirm the mean transport value estimated by Whitworth and Peterson (1985) but have not demonstrated the observed variability, especially on very short time scales. The two jets, as the name implies, contain the water that has the highest velocity in the ACC. Therefore, the greatest part of the transport will be found within them. At Drake Passage, 75% of the 130 Sv transport is located within

the jets while they only occupy about 25% of the cross-sectional area of the passage (Whitworth, 1988).

The water in the Southern Ocean is very dense and comes from different sources. Figure 1.3 presents the different waters identified across Drake Passage (Whitworth, 1988). Most of the water north of the polar front is thought to not be of Antarctic origin. For example, the Circumpolar Deep Water's high salinity can be traced back to outflow from the Mediterranean Sea and North Atlantic Deep Water (*e.g.*, Whitworth, 1988) . This inflow of waters with very distinct properties creates a particular density structure for Drake Passage. Figure 1.4 presents the potential density profile across Drake Passage. We can see from figure 1.4 that the isopycnals rise in a series of steps as we go poleward. The regions of maximum slope in the isopycnals define fronts. Such density profiles have been observed very much throughout the whole course of the ACC (WOCE D.I.U., 1998). This frontal structure is therefore believed to circle the Antarctic. There are two major fronts in the Southern Ocean and each is associated with an ACC jet. The polar front is associated with the innermost of the two ACC jets. This front can easily be measured since the potential density change we see in figure 1.4 is associated mainly with a large temperature change. The subantarctic front, on the other hand, is a little harder to identify, since its surface temperature remains fairly constant. This frontal structure causes the appearance of the two jets as water parcels tend to try to conserve their potential density. As meridional displacements are associated with large changes in potential density near the fronts, we have here the explanation for the presence of the jets. It is easier for the water that is "trapped" in the fronts to move along it rather than across it and this is true for the whole water column (ref. figure 1.4). This confinement is also the reason why the water characteristics are quite uniform throughout the flow of each jet.

These velocity values, combined with the latitude circle length of 24,000 km at about 50°S, let us estimate the period of revolution of a parcel at the surface at

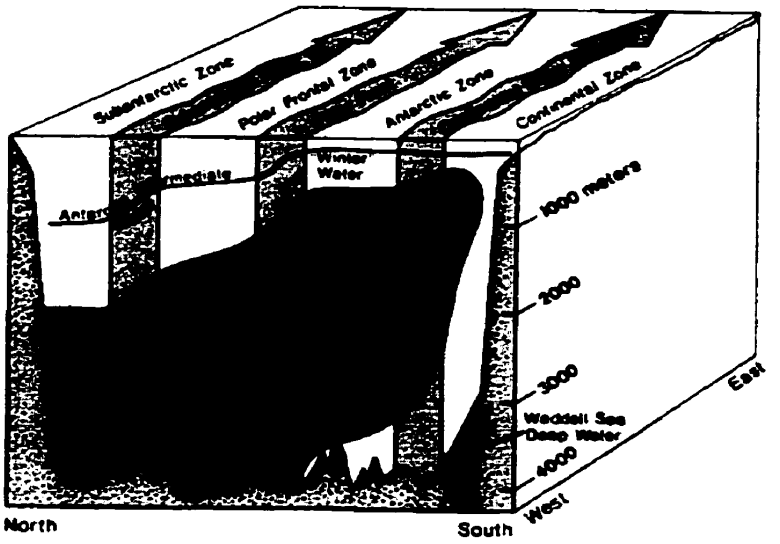

Figure 1.3: The zonation of the Antarctic Circumpolar Current at Drake Passage and the principal water masses of the Southern Ocean. (Reproduced from Whitworth, 1988.)

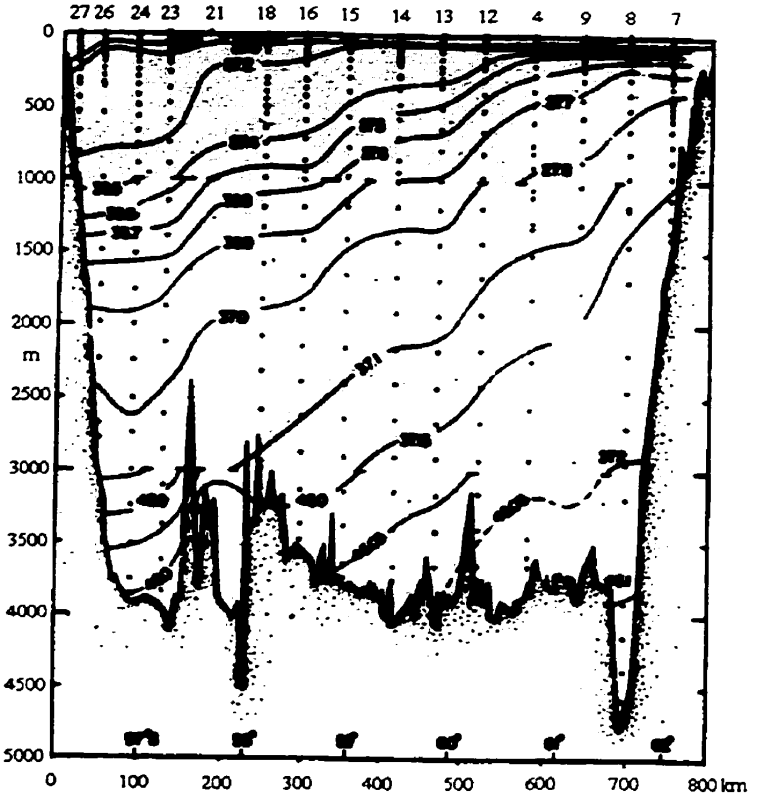

Figure 1.4: Section of variability referenced density parameter σ across Drake Passage calculated from *Melville* Section II FDRAKE 75 data. Dots identify location of moorings. Figure 4 from Nowlin *et al.* (1977).

about 500 days. It therefore takes a water parcel less than a year to move from one of the three major oceans (Pacific, Atlantic and Indian) to the next. This short travel time, combined with the size of the ACC transport, makes it easy to see that the ACC plays a major role in the transfer of water properties between ocean basins. This also means that the Antarctic Circumpolar Current possesses the potential for widespread distribution of pollutants across the Southern Hemisphere. The ACC is also suspected to play an important role in the thermohaline circulation (Toggweiler and Samuels, 1995). The path of thermohaline circulation (THC) conveyor belt flows, in its southern branch, through part of the ACC path. This raises the question as to how these two circulations interact. Is the constant input of Circumpolar Deep Water and Antarctic Intermediate Water by the thermohaline circulation driving part of the ACC or might it be the other way around? Recent numerical experiments show that blocking Drake Passage tends to shut off the thermohaline circulation (Toggweiler and Samuels, 1998). While there is no contest that the major driving force of the ACC is the mid-latitude westerlies, the impact of the THC could be fairly significant in the structure and path of the ACC as the frontal structure we have seen earlier is a direct result of the input of dense water from the mid-Atlantic (Whitworth, 1988; Toggweiler and Samuels, 1995).

Studying the ACC is more than a purely theoretical question. As we have seen, the enormous transport associated with the current can serve as a connector between the world's ocean basins. Heat, salt, nutrients or pollutants can be redistributed fairly quickly, in a few years, from one basin to the next. This can have important implications when dealing with global circulation models or global climate models as the Southern Ocean dynamics need to be well understood to obtain good results for the southern part of the Southern Hemisphere.

1.2 Understanding Southern Ocean flow

Stommel (1957; 1962) was one of the first to attempt to formulate a theory of Southern ocean flow. He suggested that a southward Sverdrup transport into the Southern Ocean accounts for the transport through Drake Passage. The ACC is therefore viewed as a warped subpolar gyre. Recall that Sverdrup dynamics, which can be applied directly to mid-latitude gyres, require the presence of eastern and western boundaries to the flow. Such boundaries are provided by continental shores and serve to establish a zonal pressure difference which drives a geostrophic flow to balance the Ekman pumping induced by the eastward winds.

In the case of the Southern Ocean, the western boundary is the southeastern coast of South America (see figure 1.1). The eastern boundary can be taken to be formed of the southwestern coast of South America and the western side of the Antarctic Peninsula. There is therefore a gap in the eastern boundary, namely Drake Passage. This allows for the flow to evolve differently from mid-latitude gyre dynamics. The return flow needed to feed the western boundary current is now an eastward flow through the gap instead of a westward flow in the basin. If there were no gap, we would expect the Southern Ocean current to form a very elongated gyre. This view of the ACC is supported by the large southward deviation of the flow along its path. The ACC evolves from about the 45°S parallel near the western boundary to the 60°S parallel as it closes its path through Drake Passage.

Baker (1982) calculated the southward transport across the 55°S latitude circle from the wind stress curl over that same circle. He assimilated the southward transport value to the Drake Passage transport and obtained a Drake Passage transport of 169 Sv and estimated the error in this estimate (due to wind field uncertainty) to about 50% of the transport value. His estimated transport is consistent with the measured transport values. This estimate was done over by Godfrey (1989) with a more recent wind stress field (Hellerman and Rosenstein, 1983) and he obtained a

slightly smaller transport value of 128 Sv. However he performed his calculations on the 54°S latitude circle. Chelton *et al.* (1990) used the same data and obtained 114 Sv for the 55°S latitude circle. They attributed the difference with Godfrey's value to their smoothing of the wind stress field. Warren *et al.* (1996) calculated a southward transport value of 130 Sv at a latitude of 60°S, again using the same wind stress field. The errors in these estimates still remain quite large. Also, one must note that the relative agreement between all of these values might be purely coincidental. There is no obvious reason why the southward transport should be calculated across a particular latitude circle. Nonetheless, these values give rather strong support to the Sverdrup-dynamics in relation with ACC flow.

Numerically, the ACC was first studied using simple basin and channel models and later with more realistic general circulation models (GCM). Channel and basin models were used for analytic simplicity. They allowed for a better understanding of the Drake Passage latitude band dynamics while demanding less computer resources than GCMs. At first, numerical ACC models provided model transports that were largely dependent upon the horizontal eddy friction coefficient value that was used. The first such numerical model studies (*e.g.*, , Hidaka and Tsuchiya, 1953, Gill, 1968) done for the Southern Ocean gave ACC transport values that were about three to four times the observed values. The only way to obtain reasonable transport estimates with these models was to incorporate an unrealistically high bottom friction or to use lighter winds than observed. Gill and Bryan (1971) developed an ACC model in which a basin was zonally connected by a gap in the eastern and western walls. The gap was a simple representation of Drake Passage. The transport value was dependent upon the gap being open all the way to the bottom or not and varied greatly between the two cases.

As the computer resources expanded, more realistic simulations of the Southern Ocean were attempted. The coarse resolution models of the late 1970's obtained results which were in fairly good agreement with measurements. In the late 1980's,

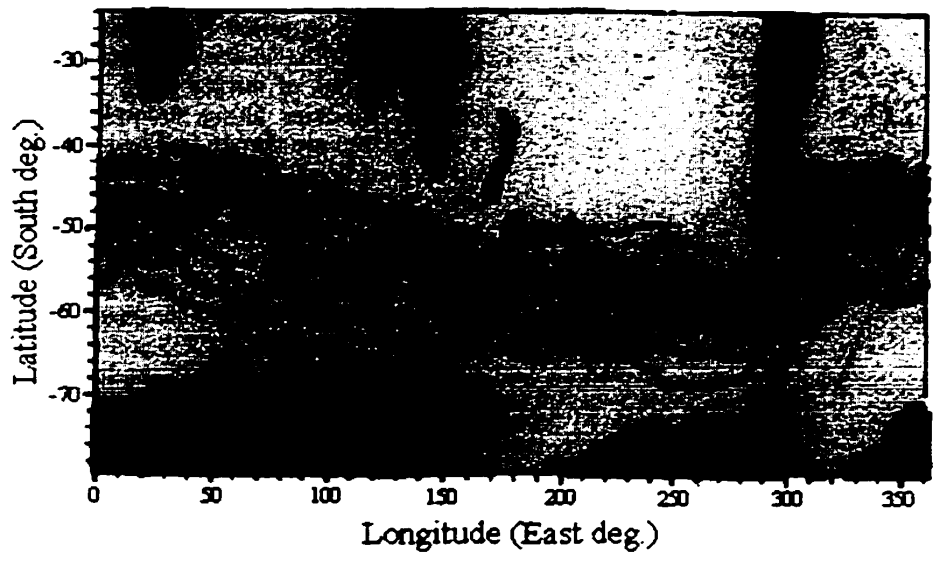

Figure 1.5: Antarctic Circumpolar Current path given by FRAM results. Time-averaged barotropic streamlines ranging from 10 Sv to 170 Sv with a contour interval of 10 Sv. The 10 Sv contour is farthest north. Figure 1 from Ivchenko *et al.* (1996).

the U.K. Fine Resolution Antarctic Model (FRAM) (FRAM Group, 1991) was constructed to try to model the Southern Ocean flow more accurately. FRAM was based on the 1984 Cox primitive equation model and run at near-eddy resolution. It is a 32-level model with a spatial resolution of 0.5° in longitude and 0.25° in latitude. The model was spun up to the Levitus (1982) salinity and temperature fields and forced with observed surface stresses. After 16 years of integration, the obtained flow field resembled the observed ACC characteristics. Figure 1.5 presents the time-averaged barotropic streamfunction field obtained from this model (Ivchenko *et al.*, 1996). These results are very similar to the flow path presented in figure 1.1. The ACC transport obtained is, on the other hand, a little too high at 185 Sv but this could be due to the parameterizations of very small-scale eddies and of bottom topography. The picture depicted by the Sverdrup dynamics view of the ACC is consistent with the FRAM results, as to the path and strength of the ACC. The results also demonstrated that the Southern Ocean possessed very strong transient eddy activity.

Ivchenko *et al.* (1997) found that baroclinic instability was an important mechanism in FRAM. They found all regions of predominantly zonal flow to be baroclinically unstable.

Ishida (1994) studied the ACC flow using a barotropic channel model. This channel model had a flat bottom and two partial meridional barriers. These barriers were representative of the South American Peninsula and of the Scotian Arc, just east of Drake Passage. The model gave realistic transport values. It showed in an idealized setting that Sverdrup dynamics apply to the ACC system. However, the model having a flat-bottom, its results are probably difficult to extend to the real Southern Ocean. Remember that the Southern Ocean does not possess a quasi-permanent pycnocline, like mid-latitude basins, which shields the wind-driven circulation from the bathymetry. One therefore has to take the bathymetry into account in ACC theories. Krupitsky *et al.* (1996) developed an equivalent barotropic model of the ACC. Their model possessed realistic coast lines and bottom topography. The vertical velocity profile for the equivalent barotropic model was taken to approximate the time-mean FRAM solution (Killworth, 1995). The equivalent barotropic allowed them to study a broad range of model parameters. The equivalent barotropic model also had the advantage of being more robust to variations in model topography than the barotropic model. They were able to reproduce all the major features of the time- and depth-averaged FRAM results.

Sverdrup dynamics therefore seem to explain the path and strength of the ACC but another problem still remains: Since the Southern Ocean entirely circles the Earth in the Drake Passage latitude band, Sverdrup dynamics cannot be applied to that region. As stated before, Sverdrup dynamics require the presence of zonal boundaries to allow for a zonal pressure difference to be established. This is obviously impossible in a zonally reconnecting region. Since the wind blows over this zonally reconnecting region, it can be expected to have a contribution to the ACC transport and the total ACC flow should be a sum of the Sverdrup-dynamics and Drake Passage latitude

band portions. Therefore the channel dynamics involved need to be investigated to understand the whole picture.

The wind stress over the Drake Passage latitude band forces an eastward flow in this region. The absence of boundaries requires that another mechanism be present to allow for the removal of the wind-input momentum from the flow. Munk and Palmen (1951) introduced the concept of form drag to solve this momentum removal problem. Two types of form drag were introduced: topographical or "mountain" drag and interfacial form drag. Topographical form drag, as the name implies, is related to the presence of topography. Munk and Palmen recognized that to balance the wind stress zonal pressure differences had to appear. Thus in the absence of the usual continental boundaries another type of "boundary" had to allow for zonal pressure differences. They hypothesized that the presence of large-scale topography allowed for the appearance of these zonal pressure gradients. As water flows over topography, higher pressures tend to build upstream of the ridge or seamount. At the same time, lower pressures accumulate downstream. An along-flow pressure gradient is therefore created. In the case of the ACC, as the flow is predominantly zonal, a pattern of zonal pressure gradients is created. The zonal momentum is transfered to the solid earth and exits the oceanic system. The meridional geostrophic flow created by these pressure differences allows to close the meridional circulation by balancing the wind-induced meridional Ekman flux at the surface. Interfacial form drag works in the same way as topographical form drag except that it serves to transfer the momentum from one layer to the next in a multi-layered system. Here, interfacial displacements replace topography and this form drag allows to close the meridional circulation in each layer individually. We will expand on form drag in section 2.2.

Munk and Palmen's work influenced ACC theories for years. The inclusion of topography into the channel models caused these models to produce more realistic transport values. Several studies were therefore conducted to better understand form drag in the context of simple channel models of the ACC.

McWilliams *et al.* (1978) assimilated the Drake Passage latitude band to a zonal channel. Using a two-layer quasi-geostrophic channel model, they looked at the effect of changes in topography and basin size and also at the effect of a transient wind stress and of a partial meridional barrier. They found that the basin size and transient wind stress did not affect the solution greatly while changes in topography and the presence of a meridional barrier strongly modified the steady state solutions. They also observed that the eddy field served to transfer the momentum downwards and that the eddies were generated by baroclinic instability. Treguier and McWilliams (1990) continued to investigate the realm of possible topography and its influence on the through-channel transport. They compared the effect of random small-scale and large-scale topography and also investigated the influence of an isolated seamount in the channel center. They were limited in their investigations by the quasi-geostrophic dynamics they had chosen and which restricted the height of the model topography. Their results indicated that the mean eddy energy was more affected by topographical form drag than the transient eddy energy.

Wolff *et al.* (1991) also looked at the effect of different topographic features on channel flow. Also using a quasi-geostrophic model, they investigated more closely the relative role of standing and transient eddies in the vertical transfer of momentum. They found, like Treguier and McWilliams, that the topographic form drag had a more direct effect on standing than transient eddies.

Marshall *et al.* (1993) studied the potential vorticity budget of the Southern Ocean. They ran a three-layer quasi-geostrophic model with a realistic bottom topography and realistic coastline on the southern boundary and a vertical wall at 40°S. The model was driven with climatological winds. Their results showed that the transient eddies had to effect a northward flux of potential vorticity (across a time-mean ACC streamline). The potential vorticity sources are located south of the ACC path. This allows the eddies to provide a southward flux of heat and a vertical momentum flux. Interfacial form drag and the downwards momentum flux associated with it are

therefore associated with the presence of transient eddies.

Marshall (1995) presented an analytic model of the ACC. The model possesses realistic topography and coast lines and assumes the flow to be inviscid and adiabatic. He obtains near-zonal flow in the upper three kilometers of the ocean and topographically trapped gyres below. The modeled flow reproduces many features of the real ACC and the model is in reasonable agreement with data in giving a Drake Passage transport of 160 Sv.

Johnson and Bryden (1989) developed a simple model that predicted an ACC transport independent of friction coefficients. Their model was based on two assumptions. First, eddies transport the eastward wind stress downwards to the lower layers where topographic form drag is able to balance the transmitted wind stress. Secondly, these eddy fluxes are the result of baroclinic instability. They tested both of these assumptions against data. Briefly, their model predicts that the eastward wind stress will serve to accelerate the eastward current in the upper layers until this current becomes unstable. The eddies generated by the instability will transmit the eastward momentum downwards. When the current becomes deep enough that it reaches below the topographic height, topographic form drag can balance the eastward wind stress. They tested the model using data at Drake Passage and obtained a transport value of 96 Sv. Using slightly different hydrographic stations as their data source, the model gave a value of about 130 Sv.

Straub (1993) concentrated on the spin-up phase of a channel model and showed that, like Johnson and Bryden (1989), transient eddies were necessary in the statistically steady state. This allowed him to derive a relationship between the stratification and the barotropic zonal velocity in channel models of the ACC. This relationship can then be extended to give an estimate of the zonal transport in the class of channel models for which topography blocks geostrophic contours in the lower layer.

GCM results tend to support the idea of form drag or at least the link between topographic features and the wind stress. For FRAM, Ivchenko *et al.* (1996) determined that the main sink of wind-input momentum is topographic form drag. They analyzed the data on streamline coordinates to compensate for the deviations from a zonal flow. They calculated the interfacial form drag term, using Johnson and Bryden's (1989) quasi-geostrophic theory, in the FRAM results and proved that it can balance the wind stress. Gille (1997) investigated the Southern Ocean momentum balance using both model results and altimeter data. She used model results from the Semtner-Chervin primitive equation numerical model (Semtner and Chervin, 1992). She found that the main regions of high eddy kinetic energy were located over the three main topographic features across the ACC path. Her comparison of these results with altimeter data showed that there were in fact more regions of high eddy kinetic energy in the real ocean and that these extra regions were located over topographic features of lesser amplitude. The model probably does not resolve well enough these smaller topographic effects. All these experiments on form drag define the necessity for models of the ACC to be eddy-resolving (or near-eddy resolving *i.e.*, able to reveal but not necessarily fully resolve the eddies). As it is evident that form drag depends on the presence of eddies, these must be present in the model dynamics for form drag to balance the wind stress.

Recently, a debate over the pertinence of form drag in theorizing about the ACC started to take shape. Warren *et al.* (1996) presented an alternate perspective on form drag. They claimed that since form drag is related only to the meridional circulation, it does not have an effect on the ACC strength. They argued that as the form drag balance is equivalent to saying that the equatorward Ekman transport must be compensated by a deep poleward geostrophic current, the balance says nothing about the magnitude of the circumpolar current itself. They proposed that the Coriolis acceleration associated with the equatorward Ekman transport balanced the wind stress. As the surface stress is absorbed in a thin surface layer and the stress

divergence drives Coriolis-balanced motion, no stress is transmitted to great depth. The poleward geostrophic flow then only serves to feed the equatorward Ekman flow through upwelling. The Circumpolar Current itself has not been mentioned in this analysis and this balance is therefore irrelevant to it. Warren *et al.* also extended their reasoning to say that the study of channel models is irrelevant to ACC dynamics as they obviously cannot take into account the current's large meridional excursions. Hughes (1997) replied that, as we have seen previously, both model results and data tend to confirm the form drag theory. In FRAM, the meridional overturning occurs as small vertical excursions following isopycnals which sum up to make large vertical excursion in the zonal mean (Döös and Webb, 1994). Momentum is transfered from particles to lower particles and water particles do not actually move down from the surface to the sill depth. Interfacial form drag is therefore a real effect. The meridional circulation of momentum can therefore be closed without having particles leave the surface and move down to sill depth. This mechanism however requires that the ACC penetrate below the sill and therefore contributes indirectly to the strength of the ACC. We cannot be certain that the ACC transport will be unaffected by the form drag balance. Warren *et al.* (1997) replied that in fact, their main point was that the name form "drag" implies that this force actually decelerates the ACC which is not the case. According to them, it is therefore obscurantist to talk about this concept when theorizing about the ACC. In short, the debate stands on the fact that since the ACC strength and general path are both fairly well predicted by Sverdrup dynamics, there should be no need to invoke another mechanism (form drag) to balance the wind stress. We believe that both contributions (Sverdrup dynamics explication and Drake passage latitude band "channel" dynamics) are necessary in understanding the whole Southern Ocean dynamics. In short, as the wind blows over the Drake Passage latitude band, the fact that the ACC does not remain constrained to this latitude band does not eliminate the need to understand this region's momentum balance.

In this thesis, we will revisit Straub's view of the flow in the Southern Ocean.

We will concentrate on the Drake Passage latitude band dynamics and elaborate a theory for the zonal transport in channel models of the ACC. Our objective will be to obtain a better understanding of the contribution of the Drake Passage latitude band to Southern Ocean dynamics. Chapter 2 will present the theoretical approach. In chapter 3, we will define the numerical model used to test our hypothesis and also review the set of experiments that were conducted. The numerical results will be analyzed in chapter 4.

Chapter 2

Theory

2.1 An idealized model of the Southern Ocean

An idealized model of the Southern Ocean can be separated into two parts: a "basin" region and a channel section (see figure 2.1). Continents bound the basin section on three sides and the southern side is open. The channel section is zonally periodic and bounded on the southern side by Antarctica. The channel section is representative of the Drake Passage latitude band.

In the basin region, blocked geostrophic contours are present and classical Sverdrup dynamics can be assumed to apply. The wind stress structure at these latitudes implies an upward Ekman pumping which consequently drives a southward drift in the interior of the basin. The absence of a southern wall to the basin allows for the water to return to the western boundary layer through eastward flow in the channel section.

In the channel section, classical Sverdrup dynamics cannot be applied as there are no eastern or western boundaries to allow for a zonal pressure difference to appear.

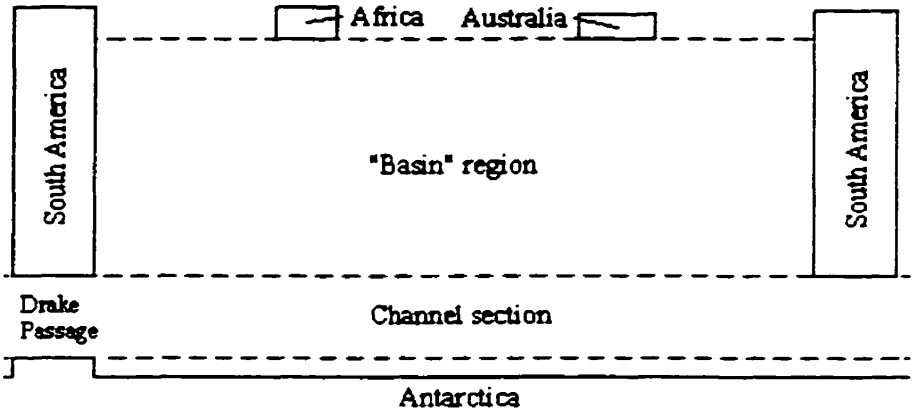

Figure 2.1: Schematics of our idealized Antarctic Circumpolar Current system.

Remember that Sverdrup dynamics directly link the zonal pressure derivative, dP/dx, to the the Ekman pumping speed, w_{ek}. In the channel section, dP/dx integrates to zero as the latitude circles close over themselves. On the other hand, w_{ek} does not necessarily integrate to zero on a latitude circle. The Sverdrup relationship cannot hold in such a case.

A portion of the transport through Drake Passage can therefore be thought of as originating from the basin-like dynamics to the north of the channel section while the rest comes from the channel dynamics themselves. The "basin" portion of the transport is expected to be roughly equal to the southward Sverdrup flux across the northern boundary of the channel section. It is therefore imperative to address the question of what dynamics control the transport in the channel section.

To investigate this question we will concentrate on the momentum balance and more specifically on what determines the zonal transport in the channel section. This will be done in the context of a simple two-layer model. We will look at the dynamics involved in the spin-up of such a two-layer channel model. This will then lead us to derive an estimate for the through-channel transport.

Our idealized channel section has the following characteristics. The ocean is rep-

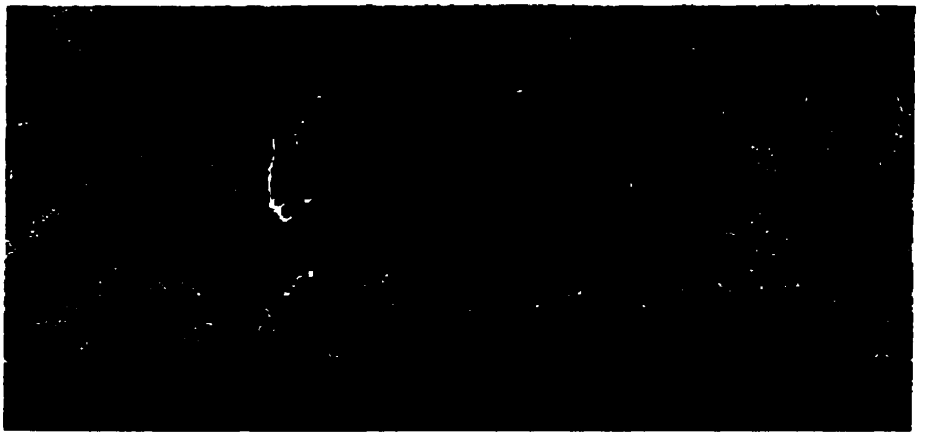

Figure 2.2: Qualitative presentation of Southern Ocean bathymetry. The darker colors indicate greater topographic features.

resented as two layers of constant densities. No exchange of water mass is possible between the layers. Vertical walls bound the channel on its northern and southern sides. The wind forcing takes the form of an eastward stress. Bottom topography is shaped as a large meridionally-blocking ridge that extends from one channel wall to the other.

This model ocean is a very crude representation of the Drake Passage latitude band portion of the Southern Ocean. The high meridionally-blocking topography assumption is supported by Southern Ocean bathymetry. Figure 2.2 qualitatively shows that the Southern Ocean is filled with high and wide topographic features. A feature like, for example, the Scotian Arc, located just east of Drake Passage, extends all the way up to a depth of 1000 m and is as wide as Drake Passage itself. The eastward wind stress magnitude is based on observations of the mean winds over this latitude band. The two-layer system is a simplified view of the Southern Ocean stratification and has the advantage of being easy to manipulate analytically. The justification of the presence of vertical walls needs further investigating to justify. We will revisit this question in section 2.4.

2.2 Concepts of form drag

Over the years, ACC dynamical theories have witnessed the appearance of various solutions to the failing Sverdrup dynamics in the Drake Passage latitude band. The absence of a western boundary in the Drake Passage latitude band or in a more theoretical zonal channel prohibits the existence of a western boundary layer to remove the wind-input momentum from the flow. Gill (1968) demonstrated that bottom stress alone could not balance the wind stress. He also calculated that a meridional flux of zonal momentum of the order of 1×10^{-2} m^2 s^{-2} across the northern and southern boundaries of the ACC would be needed to balance the wind stress. Bryden and Heath (1985) used observations to calculate meridional eddy momentum fluxes of about one quarter of the value required by Gill. They also observed that the standing eddy momentum fluxes were about half of Gill's estimate. The meridional divergence of the meridional flux of eastward momentum therefore does not seem to be large enough to balance the wind stress.

Munk and Palmen (1951) had suggested that mountain drag or topographic form drag could be the mechanism replacing the western boundary layer in the ACC dynamics. Horizontal pressure differences created by seamounts and ridges are needed to balance the wind stress. High pressures are found upstream of the ridges or seamounts as water piles up on that side. Figure 2.3 is a schematic representation of topographic form drag. In the steady state, the horizontal pressure difference (P_x) is related to the wind stress (τ^x) as

$$\oint T_x P dx = \oint T P_x dx \approx \oint \tau^x dx \tag{2.1}$$

where T is the topographic height and subscripts denote derivatives. The integrals are over latitude circles.

The left hand term is the form drag while the second term is a meridional geostrophic transport. The last term is the wind stress. Equation 2.1 shows that

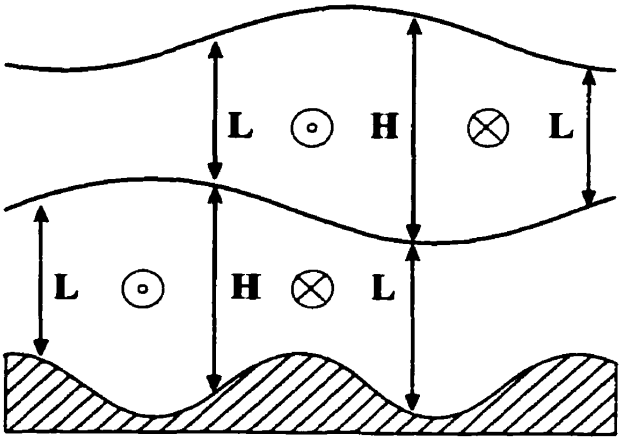

Figure 2.3: Form drag diagram. The two mechanisms (topographic and interfacial form drags) are represented in this diagram. Geostrophic currents in each layer are induced by the pressure differences (H. L) caused by the interfacial displacement (upper layer) or the topography (lower layer).

form drag corresponds to a net pressure torque. Each rise and fall of the topography either forces the flow northwards or southwards. It is the difference between these opposing flows which determines the total effect of form drag. Through this mechanism, the zonal momentum is transfered to the topography where it serves to modify the Earth's angular momentum. It is now lost from the oceanic system.

A similar mechanism can also be applied in a multi-layered system. Interfacial form drag serves to transfer momentum from one layer to the next. The balance here can be written as

$$\oint \eta_x P dx = \oint \eta P_x dx. \tag{2.2}$$

In this case the topography is replaced by the interface height, η. The crests and valley of the interface act just like bottom topography and accept the momentum from the layer above it. This momentum then serves to drive the flow in the underlying layer. Again here the form drag drives a net meridional geostrophic flux in the upper layer. We therefore have that the vertical transfer of momentum is associated with the appearance of meridional geostrophic flows in each layer.

We can separate equation 2.2 into its standing and transient parts:

$$\oint \eta_x P dx = \oint [\bar{P}_x \bar{\eta} + \overline{P'_x \eta'}] dx \tag{2.3}$$

where overbars and primes denote time averages and anomalies, respectively. The first term on the right-hand side contains the standing eddy contribution while the second term is associated to the transient eddy mean transport. Several authors (Treguier and McWilliams, 1990; Wolff *et al.*, 1991) discussed the relative importance of these two terms. They came to the conclusion that the standing eddy part was significantly larger than the transient eddy contribution and is more affected by the form drag.

2.3 Momentum balance during spin-up of a two-layer channel model

We would now like to review in a few sentences the meridional circulation of wind-driven flow in a zonal channel. Straub (1993) looked at flow in such a zonal channel from the angular momentum perspective. Briefly, he notes that the angular momentum of a parcel is dominated by its planetary angular momentum (L_P) associated with the solid body rotation component of the Earth. Meridional flow results in a change in the moment arm and hence a change in L_P. The relative angular momentum associated with eastward flow is much smaller. The total angular momentum of the two-layer system is a nearly conserved quantity while the total angular momentum in each layer individually can vary. In other words, there can be large meridional water mass fluxes in each layer but the total meridional mass flux of both layers taken together will remain close to zero. This being said, the meridional circulation is seen as an increase in L_P in the upper layer driven by the wind-stress torque and a geostrophic return flow (associated with a bottom pressure torque) in the lower layer to balance the increase in L_P of the upper layer. Then, since the angular momentum is added at the surface and removed at the bottom of the ocean, we must have a ver-

tical transfer of momentum in the steady state. This requires that the circulation be closed in each layer individually in the steady state as seen in the preceding section.

In channel models, the ability to remove angular momentum from the channel is a necessary but not sufficient condition to the establishment of a statistical steady state of wind-driven flow. This can be inferred from the fact that while a topographic form drag nearly equal and opposite to the wind stress sets up quite rapidly in the first few months of integration, the interfacial form drag will on the other hand take several years to develop. To illustrate this, we can look at transport time series from Wolff *et al.* (1991) (reproduced here as figure 2.4). These time series are obtained from runs of a two-layer quasi-geostrophic channel model with bottom topography. We see that the transport slowly increases over the first five model years before reaching the steady state. The transport would increase much faster than computed if there were no mechanisms at work to remove angular momentum from the flow. Also, a scale analysis shows that friction plays only a negligible role during spin-up. Therefore, angular momentum is being added to the upper layer and removed from the lower layer. We deduce that a topographic form drag nearly equal and opposite to the wind stress must consequently be removing the bulk of angular momentum input by the winds.

On the other hand interfacial form stress takes much longer to develop. During model spin-up, the presence of closed potential vorticity contours in the upper layer inhibits geostrophic meridional flow in that layer and therefore the geostrophic flow has to occur in the lower layer. Recall that a blocked geostrophic contour intersects a wall or another solid boundary and, for example, free flow cannot occur along it. Closed contours are contours that circle back upon themselves and zonally-reconnecting contours close by circling the Earth. Consider a zonally-reconnecting geostrophic contour, q_o, in the upper layer. We will take $q_o = f/h$ to be constant with h being the layer depth. The meridional geostrophic transport across q_o is identically

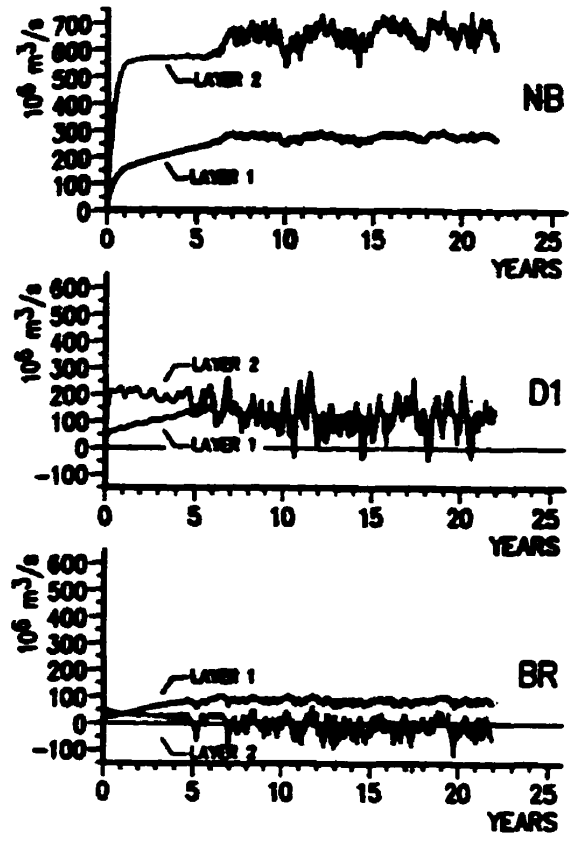

Figure 2.4: Transport time series (from Wolff *et al.* (1991), figure 9). The two upper panels are for model runs with partially-blocking meridional ridges while the lower panel results from a run with a meridionally blocking ridge. In all cases, the transport in the upper layer slowly increases until the model reaches the steady state.

zero as

$$\oint_{q_o} \frac{h}{f} P_l dl = \frac{h}{f} \oint_{q_o} P_l dl = 0 \tag{2.4}$$

where l is a coordinate following the geostrophic contour and P is the pressure. This result is valid for the latitude band which covers zonally reconnecting potential vorticity contours. It also implies that there is little vertical angular momentum transmission through interfacial form stress during spin-up as we do not have a meridional geostrophic transport in each layer (section 2.2).

The fact that the meridional circulation must be closed in each layer individually

also dictates the need for small-scale transient eddies to be present in the statistical steady state. To illustrate this, consider the circulation in the upper layer in our two-layer model. On average, the meridional geostrophic water flux across a closed geostrophic contour must remain zero. If we assume all ageostrophic fluxes other than the Ekman flux (E_f) to be zero then the mean meridional geostrophic water flux must be of equal strength but opposite direction than the Ekman flux. Consider again the closed geostrophic contour, q_o. If we take q_o to be moving with time then the geostrophic transport across q_o is now

$$\oint_{q_o} [\frac{h}{f} P_l + \mu h] dl = -E_f \tag{2.5}$$

where μ is the velocity of the contour perpendicular to itself. If E_f is different from zero then the geostrophic flux across q_o must be accomplished by the second term in equation 2.5 as the first term is identically zero from equation 2.4. Note that the second term is related to the movement of q_o and therefore to the presence of transient eddies in the flow. Therefore, once transient eddies appear, there can be a geostrophic meridional transport in the upper layer to balance the Ekman flux. The meridional circulation can now be closed in each layer individually. If we assume these eddies result from baroclinic instability, we can expect the statistical equilibrium to be baroclinically unstable.

2.4 Estimate of the barotropic zonal transport in channel models

It was shown in the previous sections that the flow in channel models of the ACC can be expected to become baroclinically unstable before reaching a statistically steady state. Therefore, the flow will eventually have to satisfy the baroclinic instability necessary condition which states that there must be a reversal of the gradient of q (e.g. H/f) with depth. This occurs when the layer interface reaches a critical slope

i.e. when

$$\eta_\theta > h_2 cot\theta \tag{2.6}$$

where η_θ, h_2 and θ are the meridional interfacial slope, the lower layer thickness and the latitude, respectively.

We can question the validity of having vertical walls in the model since the presence of the blocked geostrophic contours depends on them. These walls are, of course, not present in the real ocean. It is however to be expected that there cannot be circumpolar flow in the real abyssal ocean due to the presence of very large topographic features (figure 2.2). The blocked contours assumption therefore appears valid.

The large topography present in the model effectively blocks potential vorticity contours at depth. In the lower layer, the potential vorticity contours are deviated by the presence of topography towards the channel's northern and southern sides where they intersect the walls. The channel being periodic in the east-west direction, potential vorticity contours can close through the opening and are present in the upper layer. The presence of these geostrophic contours in the upper layer allows for the establishment of a strong zonal flow while this same zonal flow in the lower layer is essentially zero. In other words, this implies that the zonal transport is primarily confined to the upper layer where the zonally reconnecting potential vorticity contours exist.

We can use the fact that the zonal transport should be mainly confined to the upper layer along with the thermal wind relation to rewrite equation 2.6 as

$$u_1 > \frac{g'\beta h_2}{f^2}. \tag{2.7}$$

where $\beta = [\partial f/\partial y]_\theta$ and u_1, h_2 and g' are the zonal velocity, the lower layer depth and the reduced gravity in the second layer, respectively.

Then, again using the fact that $u_1 \gg u_2$, we can approximate the barotropic

velocity as $h_1 u_1/(h_1 + h_2)$. Substituting for u_1 in equation 2.7, we obtain

$$u_b > \frac{g'\beta h_1 h_2}{f^2(h_1 + h_2)} \tag{2.8}$$

or, simply,

$$u_b > \beta L_R^2 \tag{2.9}$$

where u_b is the vertically averaged (barotropic) zonal velocity, L_R is the internal Rossby radius of deformation and the h_i are the layer depths.

The right-hand side of equation 2.9 corresponds to the baroclinic long-Rossby wave speed. Therefore the necessary condition is met once the flow becomes supercritical with respect to the baroclinic long-Rossby wave speed. Although the flow only needs to satisfy equation 2.9 in a small portion of the channel to have instability occur, we will assume that the flow becomes measurably unstable over a large portion of the channel. This will allow us to use the long-Rossby wave speed as an estimate of an average value of u_b. We can consequently obtain an estimate for the zonal transport in the channel by multiplying equation 2.9 by the channel's cross-sectional area:

$$Transport \approx \beta L_R^2 (h_1 + h_2) L_y \tag{2.10}$$

where Ly is the channel width.

2.5 Implications of equation 2.10:

Equation 2.10 presents the transport in channel models of the ACC as being dependent on the square of the internal Rossby radius of deformation. We can extend this reasoning to the real ocean where the small internal Rossby radius of the Southern Ocean near 55°S implies that the contribution to the zonal transport of the zonally reconnecting part of the ACC should be minimal. At these latitudes, the internal Rossby radius if of the order of 20 km (Houry *et al.*, 1987). We can evaluate equation

2.10 using such a Rossby radius of 20 km and L_y = 750 km, h_1 = 1000 m, h_2 = 4000 m and $\beta = 1.15 \times 10^{-11}$ $m^{-1}s^{-1}$. We obtain a zonal transport value of about 20 Sv (Straub, 1993). It is important to remember that this represents but only a small contribution to the total ACC transport when compared with the 128 Sv ACC transport value estimated by Godfrey (1989) using Sverdrup dynamics in a "basin" model. Together, Godfrey's and our estimate compare well with the 180 Sv calculated using the more realistic FRAM model (FRAM Group, 1991) or the measured 130 Sv of Whitworth *et al.* (1982). In these two cases, the transport value given contains both contributions. In short, the dynamics involved here need not add significantly to the transport values calculated using Sverdrup dynamics.

Note that equation 2.10 predicts that the transport in these models should be roughly independent of the wind stress strength. The wind strength only affects the model during spin-up from a rest state. Although a greater wind stress would reduce the amount of time needed to reach baroclinic instability, the flow should always become unstable for roughly the same transport value. This independence is of course only valid for a limited band of wind stress values. One could easily visualize a sufficiently high wind stress that would induce strong enough zonal flow in the lower layer to force the appearance of zonally reconnecting potential vorticity contours. On the other hand, the wind stress needs also to be strong enough to establish a significant Ekman transport in the upper layer. Otherwise, the expected meridional circulation and the ensuing baroclinic instability would not be established. In such situations, equation 2.10 would not be applicable.

One important limitation of equation 2.10 rests in the fact that it requires that there be no zonally reconnecting potential vorticity contours in the lower layer. Consequently there can be only a small or no zonal transport in the lower layer and this requires that large meridionally-blocking topography be present in the channel. However equation 2.10 could still be applied to cases where, for example, topography would take the shape of an isolated Gaussian bump, as in the work of Treguier and

	Layer			Thermal	Our
Run	Upper	Lower	Both	wind	estimate
M1	132	112	244	104	88
M2	73	-26	47	79.5	88
BR	84	-14	70	80.5	88

Table 2.1: Comparison of zonal transport predicted by our estimate with various numerical experiments from Wolff *et al.* (1991). The thermal wind transports are calculated at $T_{r_1} - T_{r_2} H_1/H_2$ where the T_{r_i} and H_i are the two layers' respective transports and depths. All transports are in Sverdrups. (Table 1 in Straub, 1993.)

McWilliams (1990), Wolff *et al.* (1991) and others. Equation 2.10 has to be applied only to the thermal wind transport in the region over the topographic feature even though large bands of zonally reconnecting potential vorticity contours can be present elsewhere in the lower layer. The thermal wind transport is calculated assuming a lower layer at rest and using the thermal wind relation to obtain the upper-layer transport. Straub (1993) compared the estimated transports given by equation 2.10 to numerical results by Wolff *et al.* (1991). Wolff used an eddy-resolving quasi-geostrophic two-layer model to study channel flow over different types of topography. The results of these comparisons are shown in table 2.1 (table 1 in Straub, 1993). Equation 2.10 gives transport values quite similar to those from the model runs.

Also the presence of transient eddies is required by equation 2.10 to close the meridional circulation. This implies that the Drake Passage latitude band should be a zone of high baroclinicity and therefore high transient eddy activity. Observations (Bryden and Heath, 1985) and models (Ivchenko *et al.*, 1997; Krupitsky and Cane, 1997) tend to confirm this. Equation 2.10 also implies that even if the standing eddy contribution to form drag is larger than its transient counterpart (*e.g.*, Treguier and McWilliams, 1990, Wolff *et al.*, 1991) , transient eddies are necessary in the system.

In the following chapter, we will present the numerical model used to test this hypothesis. We will then describe the series of experiments that were consequently conducted.

Chapter 3

Experimental design

3.1 Numerical model

A non-linear, primitive-equation two-layer channel model with bottom topography and wind forcing was used to test our hypothesis. The model was run at near-eddy-resolving scales, sufficient to reveal although not resolve eddies with length scales comparable to the internal Rossby radius of deformation. The channel parameters were chosen to very roughly correspond to the characteristics of the Southern Ocean in the Drake Passage latitude band. As we are trying to understand the behavior of the transport value with varying model conditions, our study focused more on exploring the range of parameters for which equation 2.10 remains valid than on obtaining a realistic simulation of flow at Drake Passage.

A primitive-equation model was chosen since this allows for large topography to be used in the experiments. Quasi-geostrophic models require, by contrast, that the layer thicknesses remain close to its mean rest value throughout the integration. For example, in a two layer system, an interfacial height perturbation of the order of 20%

of the mean bottom-layer thickness is enough to call into question the linearization made in the quasi-geostrophic continuity equation. In such a case, the model would give a numerically sound but physical doubtful result. Since large amplitude topography is an integral part of the theory we are setting out to test (see chapter 2), we preferred to use the primitive equation approach. This choice was also influenced by the ready availability of our primitive-equation model.

The trade-off for this model choice was of course the greater amount of computer time required to run a primitive-equation model in comparison to a quasi-geostrophic model. In contrast with the rigid ocean surface in the quasi-geostrophic model which prohibits surface waves, the presence of a free surface in primitive equation models allows for the propagation of fast-moving surface gravity waves. A very short timestep is therefore needed to maintain numerical stability. Remember that the phase speed of surface gravity waves is given by $c_p = \sqrt{gH}$ where c_p is the phase speed, g is the surface gravity and H is the ocean depth. This results, for a typical ocean depth of 4 km and g of 9.8 m s^{-2}, in a wave speed of the order of 200 m s^{-1}. Also note that the model has to respect the CFL condition which characterizes the numerical stability of a numerical system and is defined as $C = U\Delta t/\Delta x < 1$ where C, U, Δt and Δx are the Courant number, a typical maximum velocity of the system, the timestep and the model resolution, respectively. Physically, this implies that it is impossible to resolve a wave that travels a greater distance than one gridpoint during one timestep. This is the one-dimensional criteria. In two dimensions, the model generally has to respect $C < 0.7$ but for most models people respect Courant numbers of the order of 0.4 or less. Consequently, we see that for the same model resolution and with a faster maximum wave speed U, the primitive-equation model requires a much smaller timestep than the quasi-geostrophic model to remain stable and give valid results.

3.1.1 Model formulation

The model equations are

$$u_{i_t} + \mathbf{u}_i \cdot \nabla u_i - f v_i = -\sum_{n=1}^{i} g_n \eta_{n_x} + A_h \nabla^2 u_i + \delta_{1i} \tau^x \tag{3.1}$$

$$v_{i_t} + \mathbf{u}_i \cdot \nabla v_i + f u_i = -\sum_{n=1}^{i} g_n \eta_{n_y} + A_h \nabla^2 v_i \tag{3.2}$$

$$h_{i_t} = -\nabla \cdot h_i \mathbf{u}_i \tag{3.3}$$

where subscript i denotes the layer number with $i = 1$ being the top layer and the x, y and t subscripts represent partial derivatives with respect to the zonal and meridional directions and time, respectively. Variables in bold represent vectorial quantities, u and v are the zonal and meridional velocity components, η is the interfacial or surface displacement, f is the Coriolis frequency and h is the layer thickness. δ_{ij} is the Kronecker delta. The relationships between h, η and topography are illustrated in figure 3.1. The wind stress is applied only to the first layer while the topography is constrained to the lower layer. There is no interfacial friction between the layers. The domain was defined as an east-west channel with vertical walls on the northern and southern sides. Freeslip boundary conditions were set for the two walls and periodic boundary conditions for the two open boundaries.

Calculations were made using a centered difference leapfrog integration scheme for all experiments. The model was integrated over an Arakawa C-grid for velocity and depth. The code used is based on code originally developed by Mike Davey. The Coriolis term was treated semi-implicitly. To avoid the appearance of the computational mode, an average of timesteps $n-1$ and n was performed every 31 timesteps and projected onto timestep n using a predictor-corrector scheme. This was done for both the height and velocity fields. The harmonic viscosity term is calculated at timestep $n-1$ to avoid numerical instability (Richtmyer, 1967).

The wind stress was ramped up over the first six months of integration to minimize

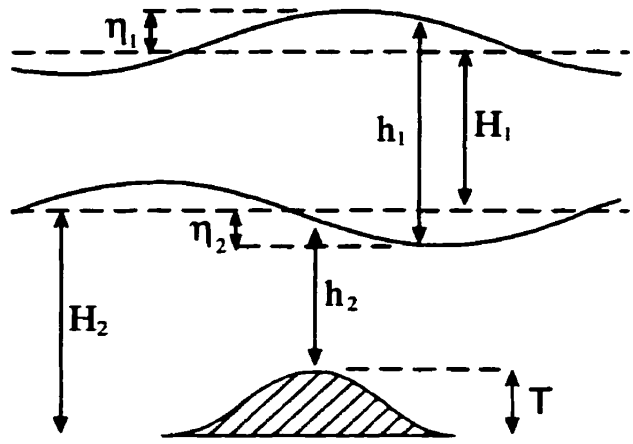

Figure 3.1: Relationship between vertical model variables. Respectively, the H_i, η_i, h_i and T are the mean layer depths, the interfacial and surface displacements, the layer thicknesses and the topographic height.

the presence of inertial waves and other spin-up problems. The model generally took three to four model years to reach statistical equilibrium and was run for about another six to seven years to obtain the time-mean flow characteristics. For our purposes, statistical equilibrium is reached when the total potential energy of the system becomes fairly constant in time as we will see in section 4.1

Numerical resolution was genrally set to 14 km. This value ensures reasonable eddy resolution for the model conditions that will be investigated. The eddy viscosity value was chosen to limit the size of the dissipation layer to just above one gridpoint. This allows it to be marginally resolved as is necessary to maintain numerical stability. It was also taken slightly greater than needed to limit the need to modify it when other parameters (for example, model resolution) are varied.

3.1.2 General parameters

The channel's zonal length was set to 1848 km while the meridional width was 840 km for all experiments. A 132 x 60 grid was used to provide a 14 km resolution.

Rest state layer depths H_i were 1000 m and 2000 m for the first and second layer respectively. A β-plane approximation was used, with f_o set to -1.1×10^{-4} s^{-1} in the meridional center of the channel and β equal to 1.4×10^{-11} m^{-1} s^{-1}, to obtain the Coriolis frequency, $f = f_o + \beta y$.

Kinematic eddy viscosity A_h was set at 280 m^2 s^{-1}. Table 3.1 summarizes the list of all parameters used in our model runs. These parameters were chosen such that the external Rossby radius of deformation was larger than the channel width.

In all experiments but one, the topography took the form of a sinusoidal meridional ridge extending from one channel wall to the other i.e. $T = T_o[1 + sin(2\pi x/L_x)]/2$ where T, T_o and L_x are, respectively, the topographic height, the maximum ridge amplitude and the channel length. The ridge height was modified for some experiments as will be presented later. This simple topography was selected as it effectively blocks potential vorticity contours in the lower layer.

The eastward wind stress (τ^x) was given a half-wavelength sinusoidal shape with a maximum value half way across the channel and assumed zonally constant:

$$\tau^x = \tau_o \sin \frac{\pi y}{L_y} \tag{3.4}$$

where y and L_y are the meridional coordinate and the channel width, respectively. Only the wind stress amplitude τ_o was varied between the different experiments. The wind stress remained constant throughout each experiment after the initial ramp to minimize inertial oscillations.

The surface gravity was chosen smaller than in reality for numerical reasons. We used 3.36 m s^{-2} instead of 9.8 m s^{-2}. A smaller surface g reduces the surface gravity wave speed and therefore allows for a 70% bigger timestep to be used (see section 3.1). On the other hand, this choice introduces a small error in the calculated flow. With a smaller g, the surface is allowed to move more freely. This therefore introduces more stretching of the water column than there should realistically be. This error is of the

Parameter	Value(s)
Channel size	1848 km × 840 km
Upper-layer depth (H_1)	1000 m
Lower-layer depth (H_2)	2000 m
f_o	-1.1×10^{-4} s^{-1}
β	1.4×10^{-11} m^{-1} s^{-1}
Resolution	12, 14, 21, 24 and 28 km
Surface gravity (g_1)	3.36 m s^{-2}
Reduced gravity (g_2)	0.022 to 0.065 m s^{-2}
Topography	500 m or 900 m sinusoidal ridge; 900 m gaussian ridge
Wind stress (τ^x)	3×10^{-8} to 1×10^{-6} m s^{-2}
Boundary conditions	freeslip at walls, periodic at openings

Table 3.1: List of all parameters used for our model runs.

same type but of opposite sign as that caused by the rigid-lid approximation used in quasi-geostrophic models. The rigid-lid approximation assumes an infinite value for g and forces the surface to always remains at its mean rest state height. It therefore reduces the amount of stretching present in the model. In our model, the rise or fall of the surface might be as large as 3 or 4 meters whereas with realistic gravity, it would probably remain around 1 or 2 meters. When compared with the upper-layer depth of 1000 m, this difference remains quite small.

3.2 Experiments

3.2.1 Dependence of transport on stratification

The first series of experiments conducted consisted in varying the internal Rossby radius of deformation (L_R) to determine the dependence of the zonal transport on stratification in these channel models. The internal Rossby radius was varied from 35 km to 65 km, typically in increments of 2.5 km. This was achieved by modifying only the reduced gravity in the second-layer while holding all other parameters fixed. A summary of chosen model parameters for each of these runs appears in table 3.2.

The wind stress maximum, τ_o, was set to 1.0×10^{-7} m s^{-2}. This value corresponds to the one used by Treguier and McWilliams (1990). Furthermore, it seemed to be a typical magnitude for the observed wind stress in the Southern Ocean (WOCE D.I.U., 1998).

The ridge height was set to 500 m to begin these experiments. This height was determined to be sufficient to block potential vorticity contours by a simple scale analysis. For the contours to be blocked, $\beta L_y / f_o$ should remain smaller than T/H_2 with f_o being the Coriolis frequency taken at the meridional center of the channel. For our parameters, the ratio of $\beta L_y / f_o$ to T/H_2 comes out to 0.42. In short, the difference in potential vorticity between the top and bottom of the ridge at any latitude is about 2.3 times that between the north and south sides of the channel at a constant height. Figure 3.2 shows f/h_2 contours for the two-layer channel at rest. A 500 m ridge is present in the lower layer. We see that the contours are very effectively blocked by a ridge of this height.

Experiment	Internal Rossby radius (km)	g_2 (m s^{-2})	Ridge height (m)	Wind stress (m s^{-2})
R1	35	0.022		
R2	40	0.029		
R3	42.5	0.032		
R4	45	0.036		
R5	47.5	0.041	500	
R6	50	0.045		
R7	52.5	0.050		1.0×10^{-7}
R8	55	0.055		
R9	57.5	0.060		
R10	60	0.065		
R1H	35	0.022		
R2H	40	0.029	900	
R3H	45	0.036		

Table 3.2: Set of investigated internal Rossby radii. The Rossby radius was modified only through changes in the reduced gravity (g_2) applied to the lower layer.

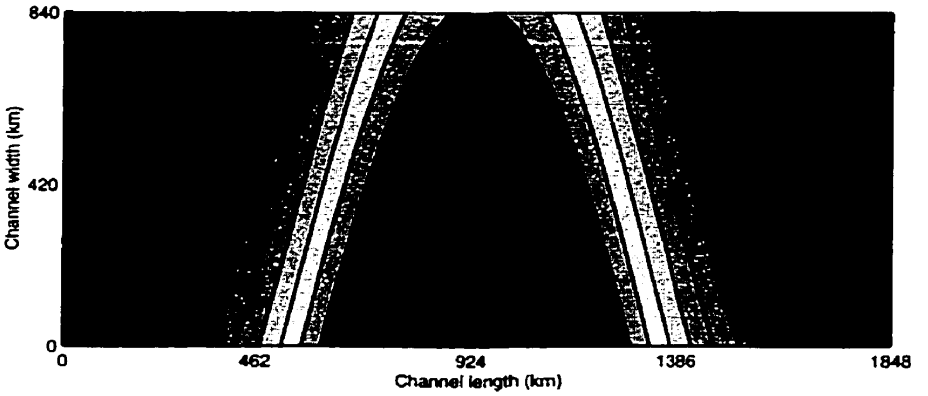

Figure 3.2: Potential vorticity contours in lower layer for a 500 m sinusoidal ridge. The fluid is taken to be at rest. There are no closed contours present in the channel's lower layer Contour interval is and the southernmost contour is .

3.2.2 Influence of the topographic height

While the absence of zonally reconnecting potential vorticity contours in the lower layer was expected with chosen model parameters, greater blocking might have an effect on the flow structure. Three runs were consequently made for L_R = 35, 40 and 45 km (runs R1H, R2H, R3H, see table 3.2) with a topographic height of 900 m instead of 500 m to examine the influence of higher topography and therefore greater blocking on the results. With a 900 m ridge, the ratio of $\beta L_y/f_o$ to T/H_2 comes out to 0.24 so we should have more than doubled the strength of the blocking. This may become an important issue when stronger wind stresses are applied.

3.2.3 Dependence of the transport on wind stress strength

A second series of experiments was conducted to determine the dependence of the zonal transport on wind stress strength as described in table 3.3. Again, the same sinusoidal wind stress shape was maintained for all runs and only the amplitude was varied. A Rossby radius of 45 km was chosen for all of these model runs, along with

a ridge height of 900 m. The greater ridge height was used to allow for a greater range of wind stresses to be applied as a greater flow speed might force unblocked f/h_2 contours to develop more easily in the lower layer with the smaller ridge.

3.2.4 Dependence of the transport on model resolution

Next, experiments were conducted to determine the robustness of our results to model resolution. The internal Rossby radius of deformation was set to 35 km, the wind stress to 1.0×10^{-7} m s^{-2} and the ridge height to 900 m. The timestep used was also maintained constant. Five model resolutions of 12, 14, 21, 24, 28 km were investigated as presented in table 3.4.

3.2.5 Other model runs

Another model run was made to test the results' sensitivity to the ridge shape. Run G1 presented a Gaussian-shaped ridge of 900 m height instead of the usual sinusoidal-shaped ridge. All other parameters were identical to those in run R2H.

Experiment	Wind stress maximum (m s^{-2})	Internal Rossby radius (km)	Ridge height (m)
W1	0.3×10^{-7}		
W2	0.5×10^{-7}		
W3	1.0×10^{-7}	45	900
W4	2.5×10^{-7}		
W5	5.0×10^{-7}		
W6	10.0×10^{-7}		

Table 3.3: Description of wind stress dependence experiments.

Experiment	Model resolution (km)	L_R (km)	Ridge height (m)	Wind stress (m s^{-2})
M1	12			
M2	14			
M3	21	35	900	1.0×10^{-7}
M4	24			
M5	28			

Table 3.4: Description of model resolution experiments.

Chapter 4

Results

4.1 Standard run

To simplify the analysis, we will define experiment R4 as our standard run and use it to understand the results from the other runs. Experiment R4 has a 500 m ridge, 45 km internal Rossby radius and 1×10^{-7} m s^{-2} wind stress amplitude. Other parameters used for experiment R4 can be viewed in tables 3.1 and 3.2. We will first describe the timeline of our standard run. Then, we will define the two through-channel transport values used in our analysis. Finally, we will expand on the flow characteristics in more detail.

4.1.1 Model timeline

Briefly, the standard run is composed of three phases: the model spin-up, the onset of baroclinic instability and the statistical steady-state. Let us first concentrate on the spin-up portion. In the case of run R4, the spin-up phase spans approximately the first 1.5 model years (540 days). The spin-up phase presents essentially zonal

flow in the upper layer and almost no zonal transport in the lower layer (figure 4.1 a, d). Flow in figure 4.1 follows the pressure contours with parcels flowing with lighter colors (i.e. higher pressures) on their left. We also see that the upper layer transport is increasing slowly with time during spin-up (figure 4.2 d). This is consistent with Wolff's transport time series (figure 2.4) and expected by our theory. The total potential energy of the channel also grows throughout the spin-up phase. The interfacial slope between the two layers steepens and provides the increased available potential energy. Once the system attains sufficient interfacial slope and available potential energy, baroclinic instability occurs and the statistical equilibrium can be reached. For our purposes, statistical equilibrium is attained when the zonal transport becomes fairly constant over time.

The moment of baroclinic instability onset is determined by a combination of factors. Snapshots of the flow during this phase can be seen in figure 4.1 (b) and (e). It is at the onset of baroclinic instability that the interfacial slope stops increasing at a constant rate. The transformation of available potential energy into eddy kinetic energy by the baroclinic instability process translates into a leveling off of the potential energy in the lower layer. Figure 4.3 presents the potential energy time series and defines the three phases. We see that after about two years, the time series starts to exhibit increased variability linked with the appearance of eddies. It then levels off around an equilibrium value. A similar signal can be found in the lower layer transport time series. Figure 4.2 (d) presents the zonal transport time series for both layers. The through-channel zonal transport is calculated as the transport across a single meridional channel cross-section. The cross-section we used is located near the western opening of the channel. For the upper layer, the zonal transport starts to exhibit more variability after 540 days and decreases back down to its equilibrium value over approximately the next 300 days. In the lower layer, we see that the transport remains almost zero during spin-up. The end of the spin-up phase is marked by a sharp increase in the variability of the zonal transport. The appearance of eddies

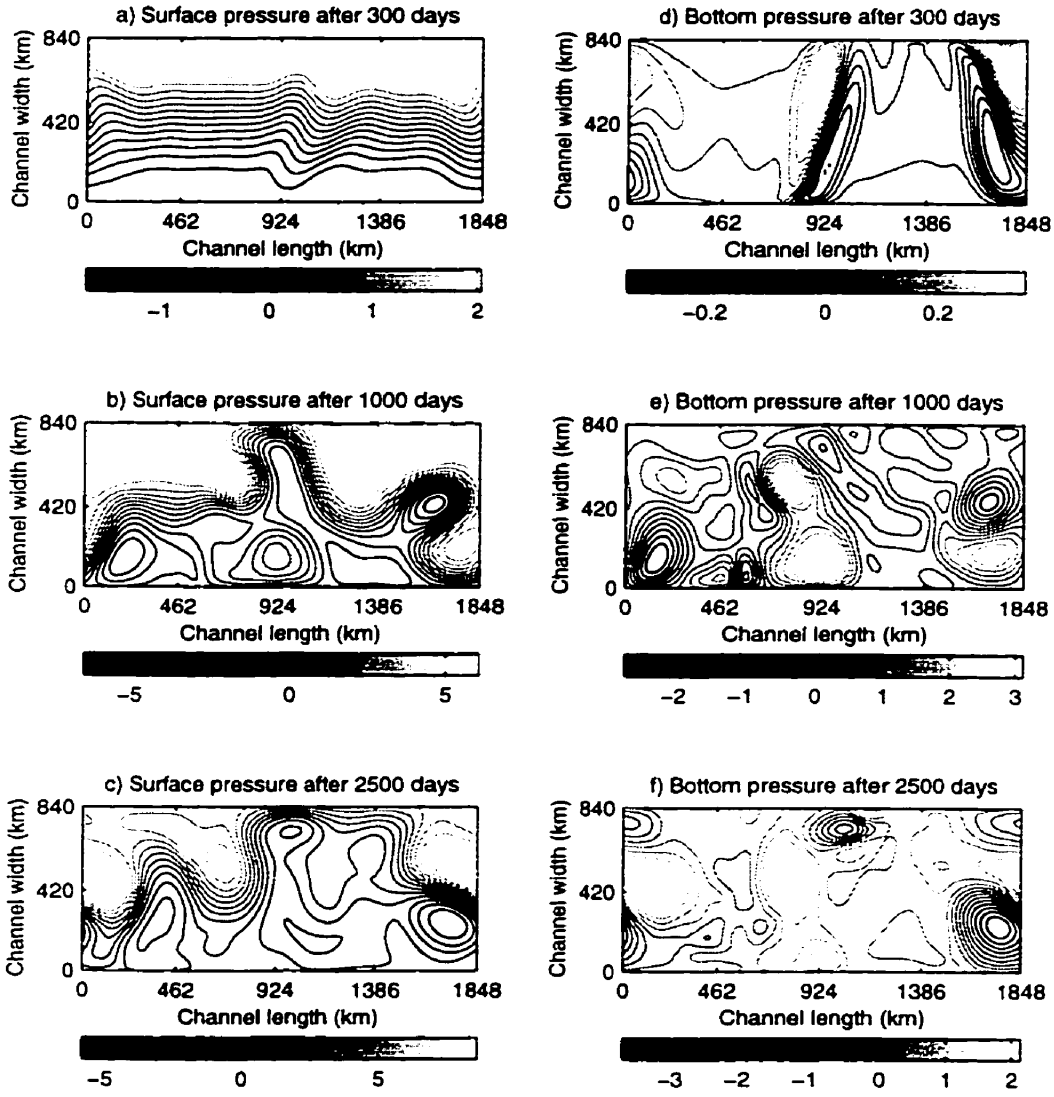

Figure 4.1: Snapshots of pressure fields from standard run. Left column: Surface pressure fields after a) 300 days, b) 1000 days and c) 2500 days. Right column: Bottom layer pressure fields after d) 300 days, e) 1000 days and f) 2500 days. The top panels are therefore taken before baroclinic instability occurs. The middle panels are just after the onset of baroclinic instability and the lower panels are taken after the model has reached statistical equilibrium. Pressures are in m s^{-2}. Shaded scales indicate range of values from lighter to darker contours. There are 15 equally-spaced contours in each panel.

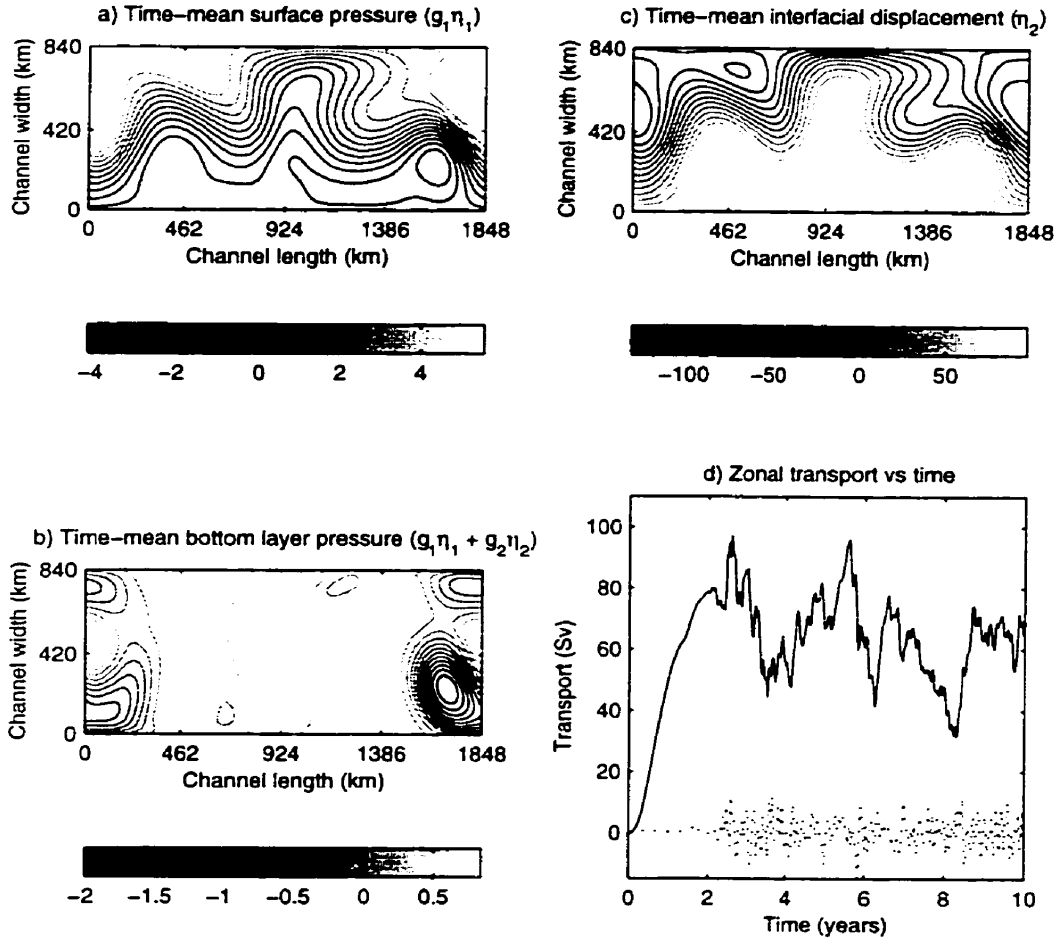

Figure 4.2: Time-mean fields for standard run: pressures and zonal transport. a) Time-mean surface pressure field. Pressures are in m s^{-2}. b) Time-mean bottom pressure field. c) Time-mean interfacial displacement. Height is in meters. d) Zonal transport time series for each layer (Solid line: upper layer, dashed line: lower layer). Shaded scales and number of contours in each panel are the same as in figure 4.1.

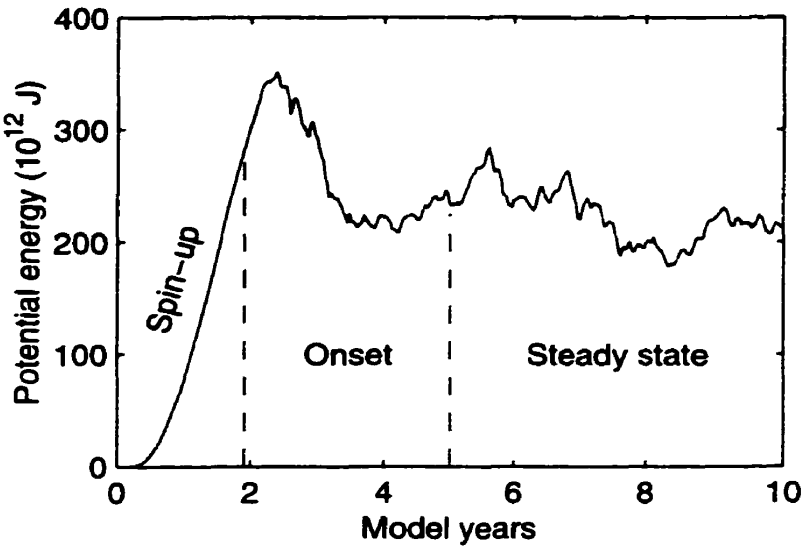

Figure 4.3: Time series of potential energy in the lower layer for run R4. The dashed vertical lines separate the three model phases.

in the lower layer causes this variability in the transport values since we now have a transient zonal flow component associated with the eddies. Therefore, depending upon the eddy field present in the lower layer, we may have periods of predominantly eastward or westward flow across the meridional line over which the zonal transport is calculated. The onset of baroclinic instability is therefore taken to be simultaneous to the appearance of variability in both the potential energy and transport time series.

One assumption made to obtain equation 2.10 dictates that a large portion of the flow must satisfy the baroclinic instability necessary condition. Figure 4.4 shows the meridional band for which the zonally-averaged barotropic zonal velocity exceeds the baroclinic long-Rossby wave speed. Figure 4.4 is obtained from run R4 after 600 days of integration i.e. about at the onset of baroclinic instability. About 50% of the channel width satisfies the condition at this time. A large portion of the channel can therefore be expected to become baroclinically unstable at the same time and our assumption seems valid. The velocity seems to have to exceed the long Rossby wave speed by a significant amount before the flow becomes unstable. This is most probably due to the presence of viscosity in our model. We can note that

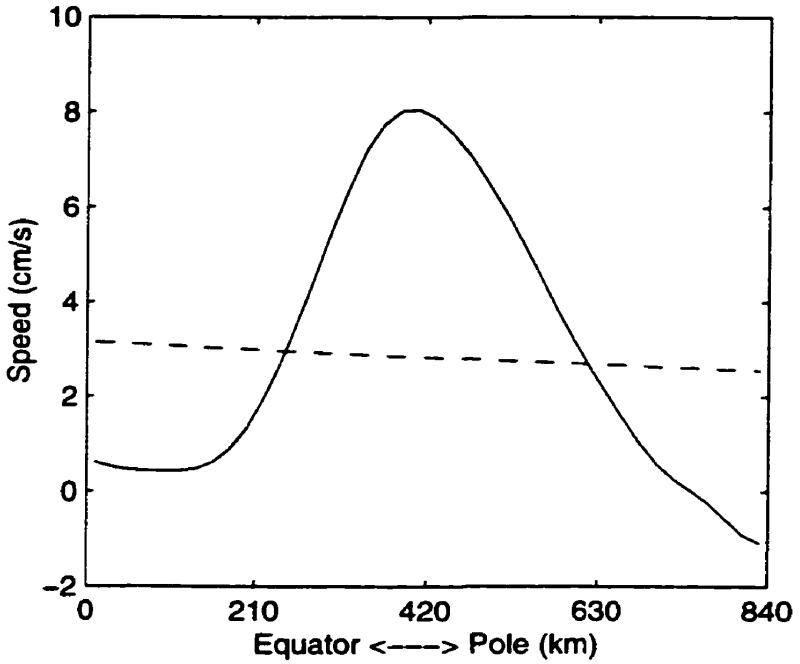

Figure 4.4: Channel meridional band over which baroclinic instability necessary condition is met. The solid line is the zonally-averaged barotropic zonal velocity and the dashed line is the baroclinic long-Rossby wave speed. Results are from the standard run after 600 days of integration.

the meridional average of the zonally-averaged barotropic zonal velocity comes out to 2.98×10^{-2} m s^{-1} while the meridional average of the long Rossby wave speed is 2.83×10^{-2} m s^{-1}. As a whole, flow in the channel is therefore close to the long Rossby wave speed and the through-channel transport estimated using equation 2.10 should agree well with the model transport at the onset of baroclinic instability.

Statistical equilibrium for the standard run is taken to begin after 1800 days. All time-mean calculations are therefore calculated over a 5 years interval (1800 to 3600 days). The zonal transport varies by approximately 20% about its time-mean value during this portion of the time series (figure 4.2 d).

4.1.2 Transport values

Two zonal transport values are extracted from each model run to be used in the evaluation of equation 2.10. The first is the transport value at the onset of baroclinic instability and the other is the statistical steady-state value. The baroclinic onset transport value will hereafter be denoted as the "critical point" transport. The barotropic transport is taken to be the upper layer transport only. In both cases, the lower layer transport is less than 2% of the upper layer transport which falls well below the accuracy of the measurements. Before baroclinic instability occurs, the lower layer transport reaches a maximum value of about 1 Sv while the upper layer transport is close to 65 Sv. Once statistical equilibrium is attained, the lower layer transport oscillates about zero with a mean value of a few tenths of a Sverdrup. We can consequently neglect the lower layer transport in the steady-state also.

For run R4, the critical point transport value taken to be 62 Sv while the steady state transport is about 58 Sv with a standard deviation of 10 Sv. The critical point value possesses an inherent error due to the fact that the critical point itself can only be determined arbitrarily. A small error in the critical point timing can translate into an error of a few Sverdrups in the transport value.

Comparing the zonal transport value predicted by equation 2.10 to the baroclinic instability onset transport value seems more natural as the theory was derived from the baroclinic instability necessary condition. Indeed, we have seen in the previous section that the agreement between theory and numerical model should be quite good near the baroclinic instability onset. Nevertheless, it is also important to look at the steady-state transport value as this is more relevant to the real ocean.The steady-state values should therefore allow for an easier extension of the theory to a more realistic ocean.

4.1.3 Flow features of the standard run

Different flow characteristics are observed in the two model layers. The time-mean flow in the top layer is dominated by a strong jet. Figure 4.2 (a) shows the upper-layer time-mean geostrophic contours for run R4. In the lower layer, there are no strong zonal flow patterns as in the top layer. Figure 4.2 (b) presents the time-mean bottom layer pressure for run R4. Essentially, we see two regions of standing eddy activity in the lower layer. We can clearly see that the eddy locations are correlated with the topography. Recall that the model ridge crest is located midway between the channel openings at the 924 km mark. The two eddy zones are located over the ridge crest and directly over the center of the valley between the repeating ridges. Standing eddies therefore seem to be largely influenced by large-scale topography as found by Treguier and McWilliams (1990) and Wolff *et al.* (1991). On the other hand, transient eddies are located fairly uniformly over the channel's central latitudes. We can see from figure 4.5 that the velocity anomaly (the time-mean value is removed) displays eddies over most of the channel. The upper panels displays no preference for particular transient eddy locations. The lower panel, associated with the lower layer fields, seems to locate more transient eddies on the western (upstream) side of the ridge. Figure 4.5 is taken from the standard run after 2600 days of integration. The fields are representative of anomaly fields taken at other times during the statistical steady state.

Figure 4.6 displays the time-mean vorticity fields for run R4. The left column presents the planetary components of the potential vorticity fields while the right column displays the full (relative vorticity included) potential vorticity fields. The upper-layer contours are zonally reconnecting and the geostrophic contours in the lower layer remain blocked with the fluid motion. The contour pattern is quite similar to that of figure 3.2. Our assumptions about the potential vorticity contour structure (zonally-reconnecting contours in upper layer and blocked contours at depth) appear

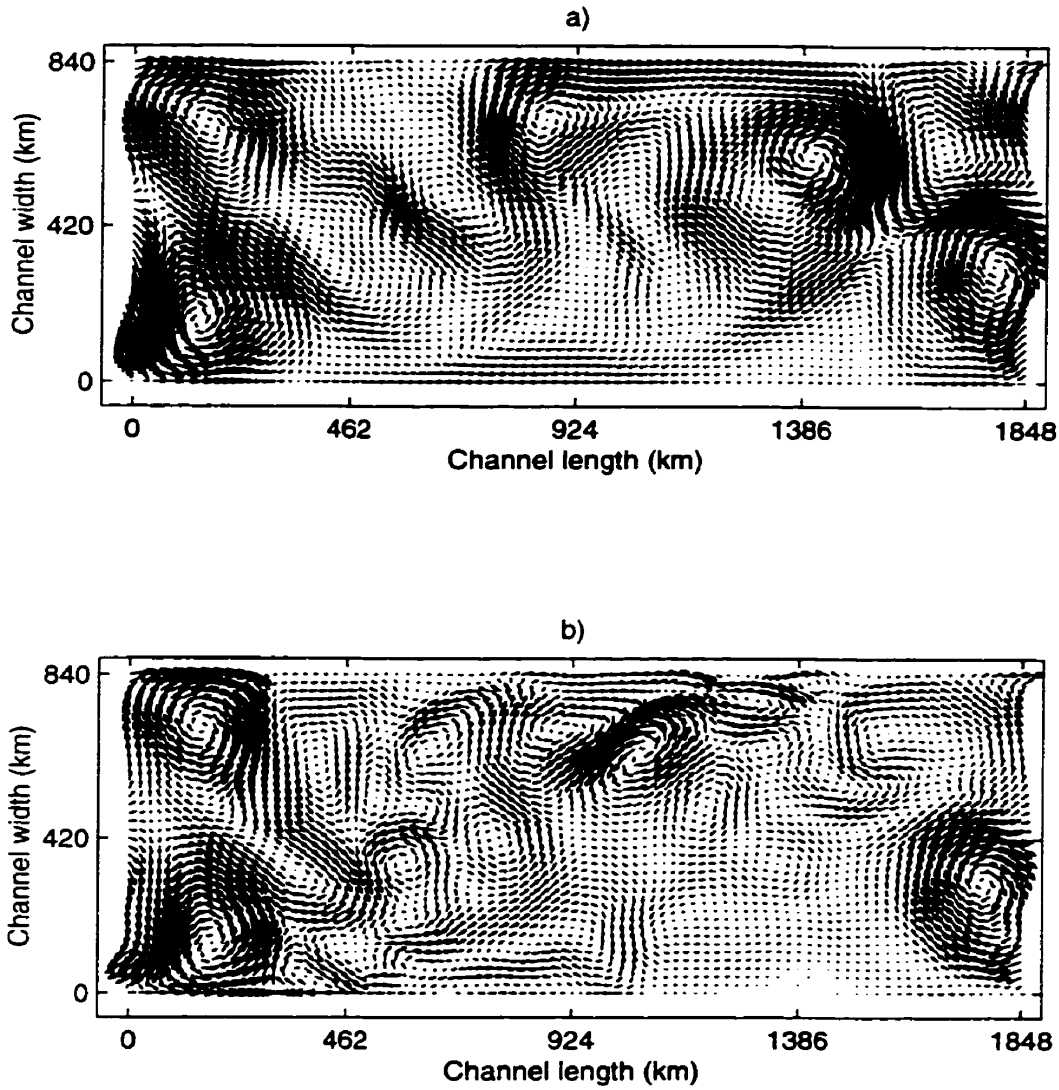

Figure 4.5: Transient velocity field after 2600 days. a) Upper layer velocities. The maximum upper-layer velocity is 79×10^{-2} m s^{-1}. b) Lower layer velocities. The maximum lower-layer velocity is 36×10^{-2} m s^{-1}.

to remain valid throughout the model run.

Figure 4.1 presents snapshots of the pressure fields for both layers at three distinct times. The upper panels (a and d) are taken during model spin-up. Panel (a) displays strong nearly-zonal flow in the upper layer while panel (b) shows no zonal flow at all in the lower layer. During spin-up, the model is building an interfacial slope sufficient to cause baroclinic instability. The velocity shear between the two layers serves to increase the interfacial slope.

To determine the importance of viscosity in our numerical model, we calculated a channel-averaged momentum balance for the time-mean flow field. Six terms remain in the balance, after the time, vertical, meridional and zonal averages of the model equations:

$$\int_{L_y} \oint_{L_x} -P_{2_x} T dx = \int_{L_y} \oint_{L_x} [A_h(\bar{h}_1 \nabla^2 \bar{u}_1 + \overline{h_1' \nabla^2 u_1'} + \bar{h}_2 \nabla^2 \bar{u}_2 + \overline{h_2' \nabla^2 u_2'}) + \tau^x \bar{h}_1] dx dy \tag{4.1}$$

where the left-hand-side term is the topographic form drag, the first two terms on the right-hand side are, respectively, the upper and lower layer standing and eddy viscosities and the last term is the wind stress contribution. P_2 is the bottom layer pressure and L_x is the channel length. These terms represent the balance between the total wind-input momentum and the topographic form drag. The transient eddy contribution to viscosity is not calculated as it is expected to be small compared to the standing eddy contribution. We present this balance to show the relative importance of eddy viscosity with respect to form drag in our results. Table 4.1 compares the four terms. Eddy viscosity is about two orders of magnitudes less than the topographical form drag and the form drag almost exactly balances the wind stress. Consequently, we can say that form drag is the principal mechanism for removing wind-input momentum in our model.

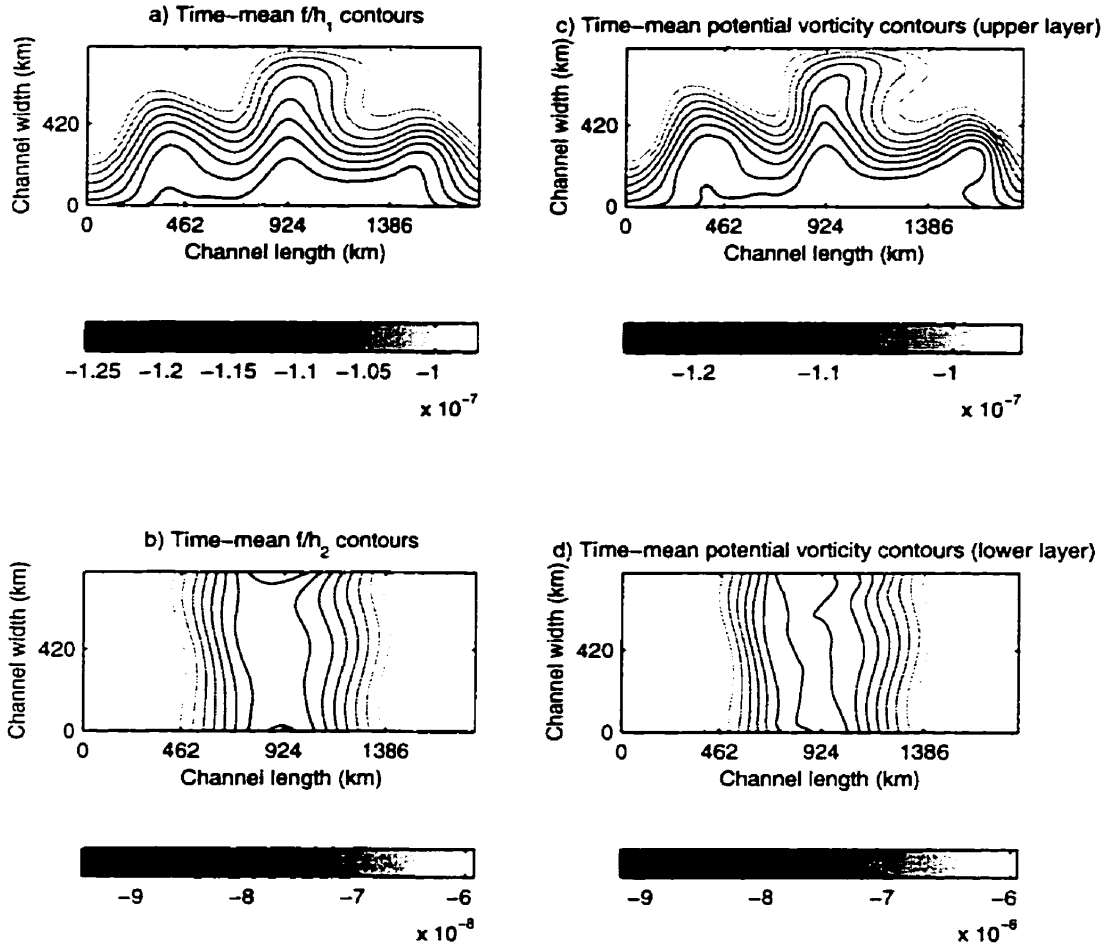

Figure 4.6: Time-mean fields for standard run: planetary and potential vorticity. Contours in m^{-1} s^{-1}. a) Time-mean planetary vorticity (f/h_1) in upper layer. b) Time-mean planetary vorticity (f/h_2) in lower layer. c) Time-mean potential vorticity (planetary plus relative) in lower layer. d) Time-mean potential vorticity (planetary plus relative) in lower layer. Shaded scales and number of contours in each panel are the same as in figure 4.1.

Term	Value ($km^3\ s^{-2}$)
Form drag	-348
Wind stress	342
Viscosity (upper layer)	-7.1
Viscosity (lower layer)	1.4

Table 4.1: Momentum balance for standard run. Numerical values of the four remaining terms in the momentum balance.

4.2 Evaluation of equation 2.10 robustness

We can now examine the results of the different series of experiments to determine the applicability and robustness of equation 2.10. Figures for each subsection will be presented at the end of that subsection.

4.2.1 Transport dependence on stratification

To evaluate the robustness of equation 2.10 to changes in the internal Rossby radius of deformation, ten model integrations were performed with different internal Rossby radii. The Rossby radius was varied by modifying the reduced gravity only. All other model parameters were kept constant (ref. table 3.2).

The flow features vary slightly from one model run to the next. Figures 4.7 and 4.8 compare the time-mean flow for runs R1 ($L_R = 35$ km) and R10 ($L_R = 60$ km). We clearly see a difference in the upper-layer jet which meanders less and is broader for experiment R1 than for R10 and also for the standard run (figure 4.2 a). The time-mean pressure field for R1 displays smaller-sized eddies than R10. These eddies are also a bit weaker in R1. While the eddies are in the same zonal locations for all experiments, their meridional extent varies. The eddies tend to be more localized

near the walls with smaller Rossby radii and expand to cover the whole basin width with the larger radii. The planetary vorticity contours maintain the same general structure in all runs. The transport time series exhibit about the same amount (20%) of variability in the steady-state. All runs exhibit increased variability after about 450 to 550 days and the baroclinic instability onset is fairly simultaneous.

Figure 4.9 presents the model zonal transports as a function of internal Rossby radius. The top panel (a) displays the critical point transport values while panel (b) presents the steady-state value. The dashed lines in both panels are numerical interpolations. The critical point transports are fitted with a quadratic function while a linear interpolation is used for the steady-state transports. In both cases, the transport values are decreasing with decreasing internal Rossby radii. The critical point transport is almost proportional to the square of the internal Rossby radius. A maximum difference of 11% between theory and model results can be seen at 60 km. Since equation 2.10 determines the transport by identifying the moment of baroclinic instability, such a good agreement can be expected. The critical point transport is, after all, the transport value at the onset of baroclinic instability.

Also, for all the internal Rossby radii investigated but one (35 km), the steady-state value of zonal transport is lower than the critical point value. Equation 2.10 can be viewed as an upper limit to the through-channel transport for that range of radii. Extending this below 35 km seems a bit hazardous as the interpolations seems to imply that the relationship should reverse. A few more experiments with smaller Rossby radii are needed to determine if this is the case. A smaller internal Rossby would probably require increased model resolution to resolve the eddies and prompted the series of experiments on model resolution.

When extrapolated to the expected Southern-Ocean internal Rossby radius of 20 km (Houry *et al.*, 1987), the critical point transport should be 17 Sv while the steady-state transport can be expected at 26 Sv. In both cases, we can say that the

contribution of such channel dynamics to the Drake Passage transport and the ACC is minimal when compared to the Sverdrup-dynamics contribution.

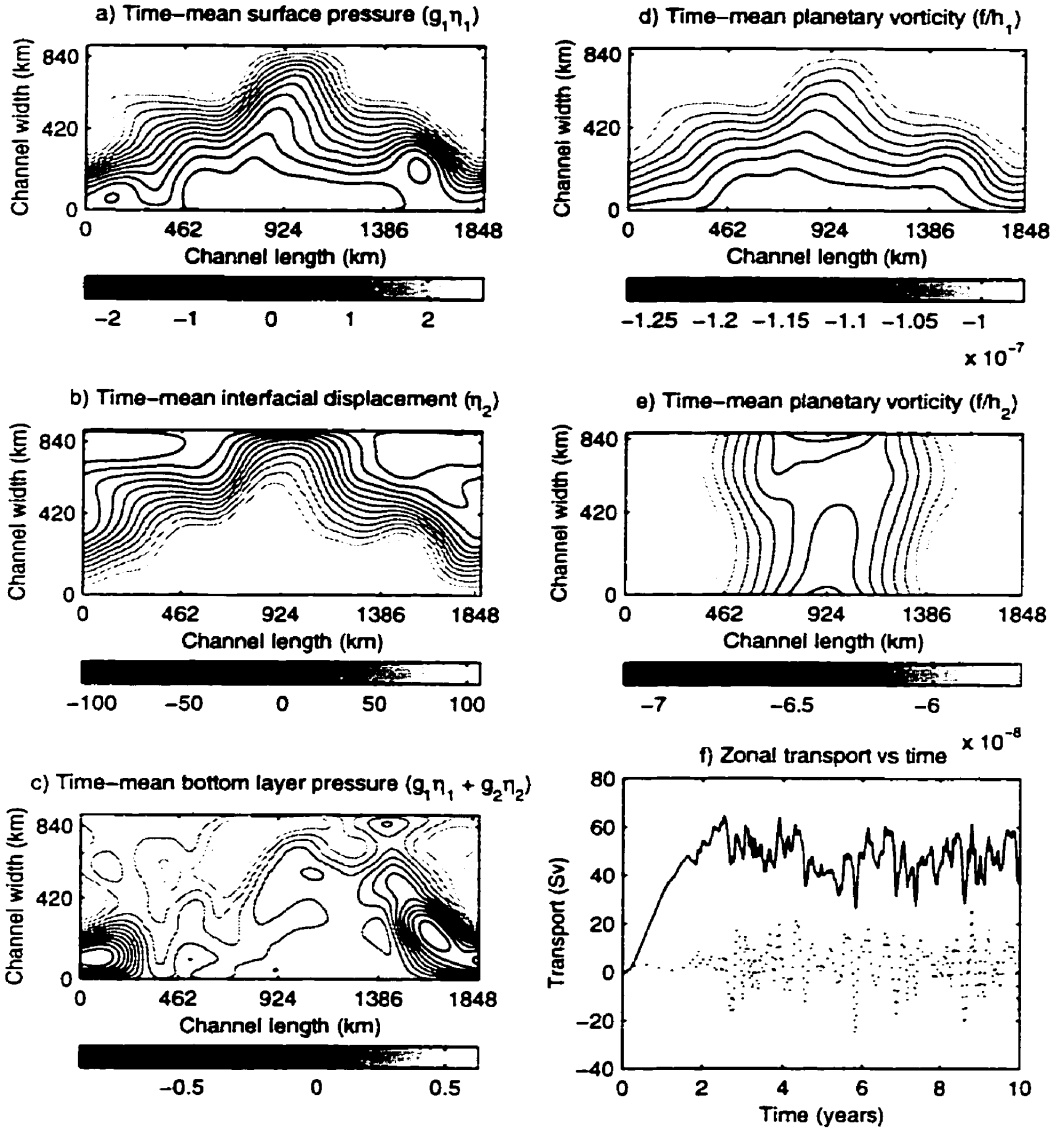

Figure 4.7: Time-mean fields and transport time series for run R1 (L_R = 35 km). a) Time-mean surface pressure field. Pressures are in m s^{-2}. b) Time-mean bottom pressure field. c) Time-mean interfacial displacement. Height is in meters. d) Time-mean planetary vorticity (f/h_1) in upper layer. e) Time-mean planetary vorticity (f/h_2) in lower layer. f) Zonal transport time series for each layer (Solid line: upper layer, dashed line: lower layer). Shaded scales and number of contours in each panel are the same as in figure 4.1.

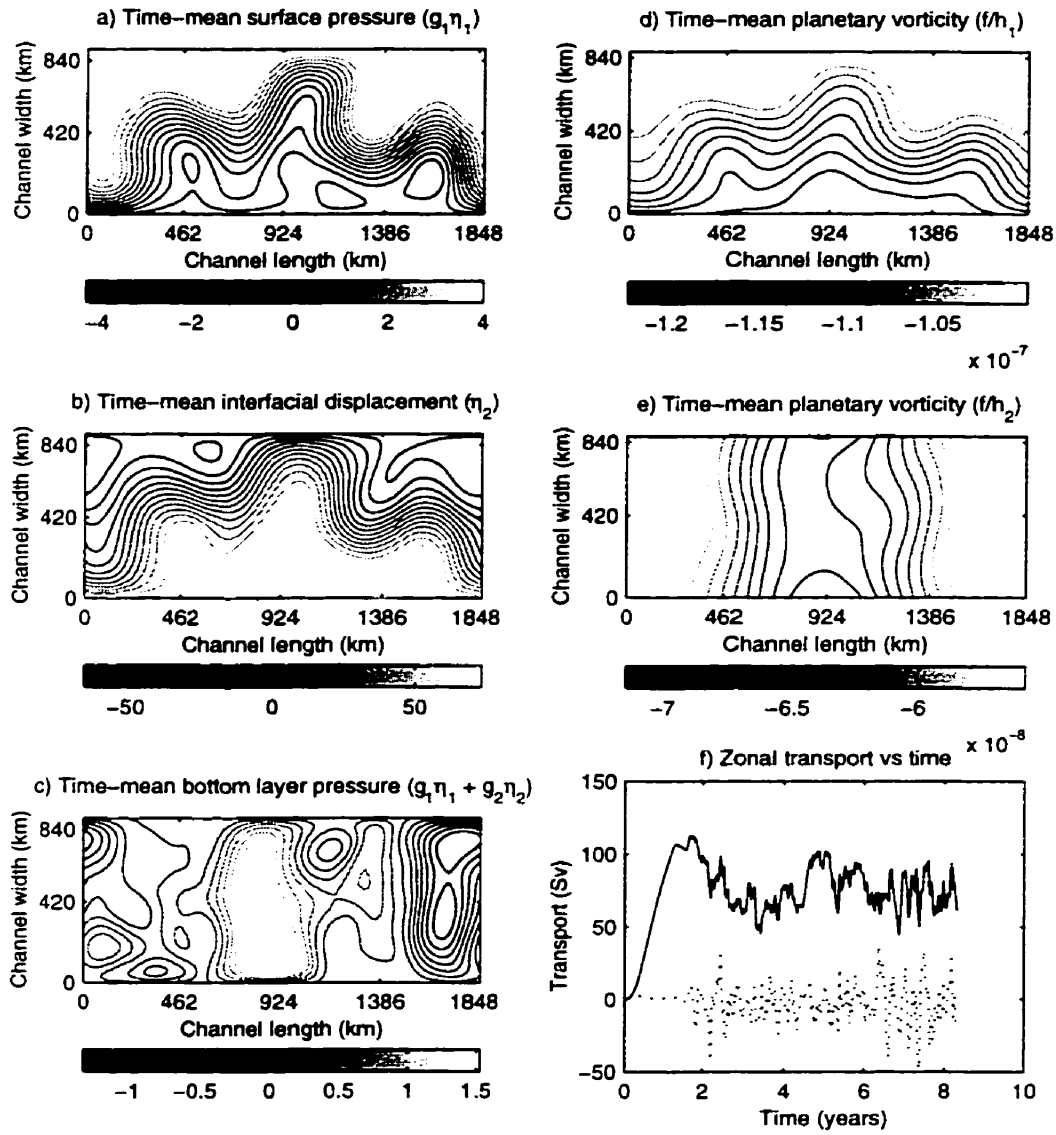

Figure 4.8: Time-mean fields and transport time series for run R10 (L_R = 60 km). Same as figure 4.7.

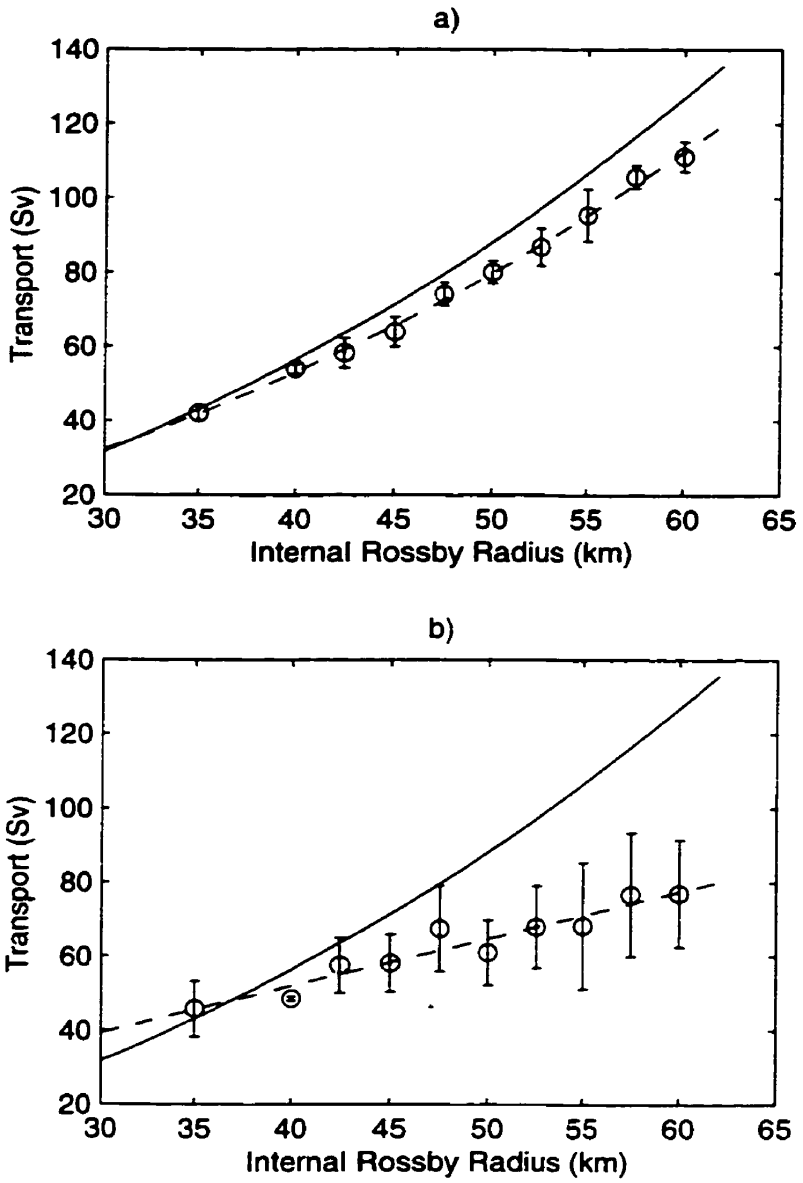

Figure 4.9: Model transports vs internal Rossby radius of deformation. The solid line in both panels is the theoretical result given by equation 2.10. a) Critical point transport values (Dashed line is quadratic interpolation). b) Statistical steady-state transport values (Dashed line is linear interpolation).

4.2.2 Transport dependence on ridge height and shape

Four experiments were conducted to determine the influence of the ridge height and shape on the results. Three experiments attempted to reproduce the results of runs R1, R2 and R4 but using a 900 m sinusoidal ridge instead of the 500 m one. The last experiment replaced the sinusoidal ridge with a Gaussian-shaped ridge.

We will concentrate first on the results of run R3H which is the counterpart of the standard run R4. The other two experiments (R1H and R2H) display similar characteristics when compared with runs R1 and R2, respectively. Figure 4.10 shows the flow fields and transport time series for experiment R3H. Clearly, the major difference between the two runs (R4 and R3H) can be seen in the pressure field. Figure 4.10 (a, c) shows that the ranges of pressures over both layers are narrower for run R3H than for the standard run. The higher topography therefore seems to cause weaker flow to appear. Aside from the strength difference, both the circulation pattern in the lower layer and the meanders in the upper-layer current are in nearly the same location as in experiment R4. An exception is that closed recirculations form in the upper layer in the standard run but not in R3H. Figure 4.2 (a) shows two large recirculation cells, one near the southern wall and one right over the periodic boundary. Westward flow being associated with part of these gyres, the through-channel transport is consequently practically the same in both runs despite the stronger upper-layer jet of run R4. The transport time series exhibit similar patterns of variability in the first six model years and attain close to the same steady-state transport value (69 Sv for R3H versus 62 Sv for R4). The critical-point transports are again almost identical (62 Sv for R4 and 63 Sv for R3H). The same transport values are therefore attained despite the generally weaker flow in run R3H. The planetary vorticity fields are again similar in both runs, with the R3H contours being slightly stronger because of the larger topography. The ridge height therefore does not seem to significantly modify the through-channel transport and we can probably expect this to hold as long as we

have such a vertical vorticity structure of zonally-reconnecting contours in the upper layer and blocked contours at depth.

On the other hand, the ridge shape seems to have a greater importance. Experiment G1 attempted to reproduce the R3H results while replacing the 900 m sinusoidal ridge with a 900 m Gaussian-shaped one. Figure 4.11 shows that the flow fields for run G1 are quite different than those of R3H. A jet is still present in the upper layer but it is now more zonal and fairly broader. In the lower layer, the time-mean pressure field exhibits two large gyres between the repeating ridges. The Gaussian ridge is much steeper than the sinusoidal ridge and in that aspect is more like a partial basin wall. At 900 m, it is also blocking almost half of the lower layer height. The flow fills the entire "basin" between the repeating ridges with two large gyres. The time-mean pressure field also still presents a large eddy located right over the ridge as in the other model runs. The vorticity structure is also accentuated. We have more zonal vorticity contours in the upper layer and more intense blocking in the lower layer. Despite these different characteristics, the presence of the Gaussian ridge does not alter the transport values much. The critical-point transport for experiment G1 is of 65 Sv while the steady-state transport jumps to 74 Sv with slightly less variability (15%). These transports are quite similar to the R3H transport values of 63 Sv and 69 Sv for the critical-point and steady-state transports, respectively. The choice of ridge shape and height therefore does not seem to influence the through-channel transport significantly.

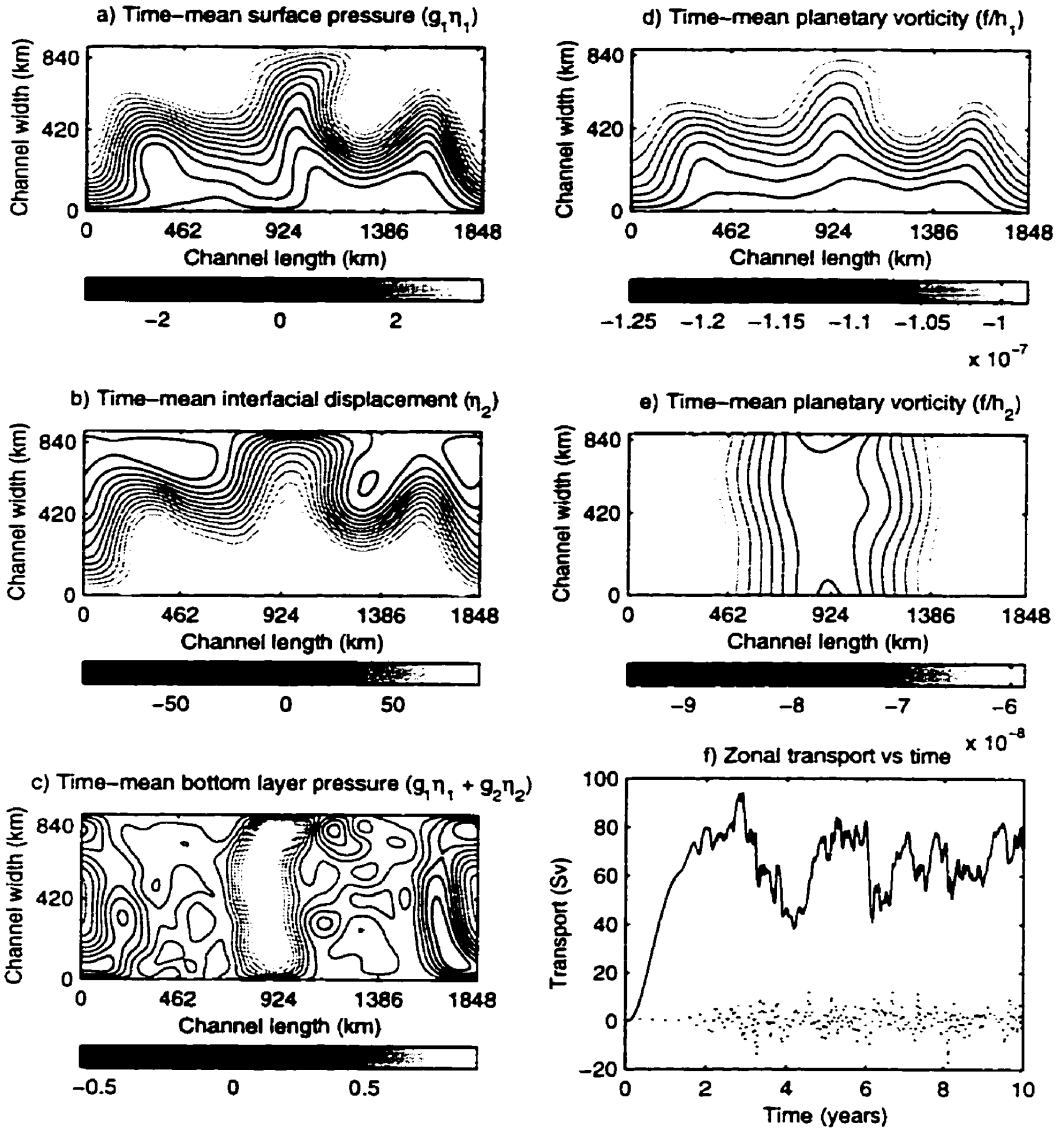

Figure 4.10: Time-mean fields and transport time series for run R3H (900 m ridge). a) Time-mean surface pressure field. Pressures are in m s^{-2}. b) Time-mean bottom pressure field. c) Time-mean interfacial displacement. Height is in meters. d) Time-mean planetary vorticity (f/h_1) in upper layer. e) Time-mean planetary vorticity (f/h_2) in lower layer. f) Zonal transport time series for each layer (Solid line: upper layer, dashed line: lower layer). Shaded scales and number of contours in each panel are the same as in figure 4.1.

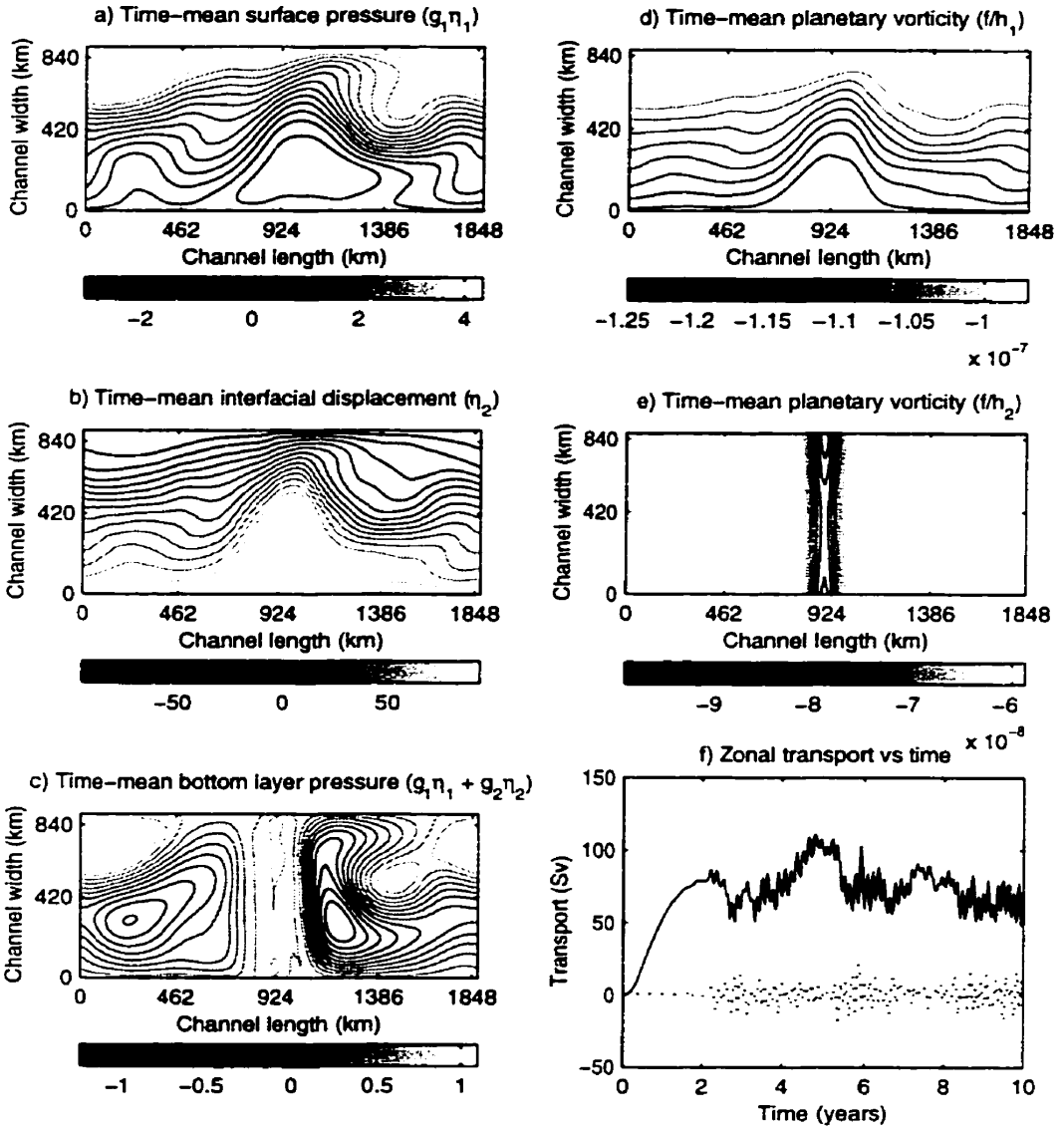

Figure 4.11: Time-mean fields and transport time series for run G1 (Gaussian ridge). Same as figure 4.10.

4.2.3 Transport dependence on wind stress strength

Six other model runs were completed to evaluate the effect of different wind stress strengths on the through-channel transport. The different model parameters for each run were presented in table 3.3. Experiment W3 is the same model run as R3H for which the results are similar to the standard run.

A smaller applied wind stress inputs less momentum into the basin. We therefore expect less eddies to be generated and for the flow to be less energetic in such a case. Figure 4.12 shows the time-mean flow fields and transport time series for run W2 in which the wind stress is half that of the standard run ($\tau^x = 2.5 \times 10^{-7}$ m s^{-2}). The general aspect of the W2 fields is similar to that of W3. The surface and interfacial displacements (panels a and b) are 25% less than for W3. Consequently, the flow velocities are quite reduced. The upper-layer jet in panel (a) also meanders less than for W3 and the standing eddy field in the lower layer, although in similar locations than that of W3, is fairly weaker. The transport time series displays less variability (only 8%)

With a stronger wind stress of 2.5×10^{-7} m s^{-2}, run W4 should display opposite characteristics to run W2 with respect to the standard run. Indeed, the W4 fields (figure 4.13) show increased eddy activity over those of run W2. Meanders in the main upper-layer jet in W2 now close into gyres in W4 (panel a). Similarly to the ridge height experiments, the transport is comparable between cases W2 and W4 because of the presence of these gyres. They cause a recirculation which reduces the through-channel transport in W4. The time-mean eddies in the lower layer are much stronger for about the same spatial coverage. In fact, the pressure fields are about five times stronger in run W4. The transport time series displays more variability than those of both W2 and W3.

The W2 transport time series shows that baroclinic instability took a longer time

to occur than for W3 but the transport value at which it occurred is similar. Run W4 reached baroclinic instability faster but at about the same transport value once again. Figure 4.14 is a plot of transport values versus applied wind stress. We see that both the critical point transport and the steady-state transport vary little for the first four experiments. Over this range, both transports increase by less than 5% while the wind stress is multiplied by five.

The last two experiments (W5 and W6) show an increase in the critical-point transport but maintain a similar steady-state transport. The increase in critical-point transport may be associated with the presence of more waves in the channel. The topography, along with the channel walls, can act as a resonance box for waves in the lower layer and the stronger wind stress may excite more modes. We can observe the presence of these oscillations in the transport time series for run W6 (figure 4.15). During spin-up, oscillations of about the same frequency as those seen in figure 4.15 can also be observed but with a much smaller amplitude. A comparison of the spin-up and steady-state power spectra (not shown) displays peaks at the same frequencies. The spin-up peak is broad and has only a small amplitude. Clearly, these results need to be considered carefully. The presence of waves in the system could affect the baroclinic instability process and consequently modify the critical-point transport. For example, baroclinic instability occurs once the system contains sufficient available potential energy. As waves require energy to propagate they would have to drain it from the available potential energy of which there consequently is less to generate instability. It would then take more available potential energy and a greater associated transport for the flow to become unstable. Also, it might just be a coincidence that the mean transports for runs W5 and W6 fall in the same range as the steady-state transports of the other four experiments. What can said for certain is that for the range covered by the first four experiments, both through-channel transports are fairly independent of the wind stress.

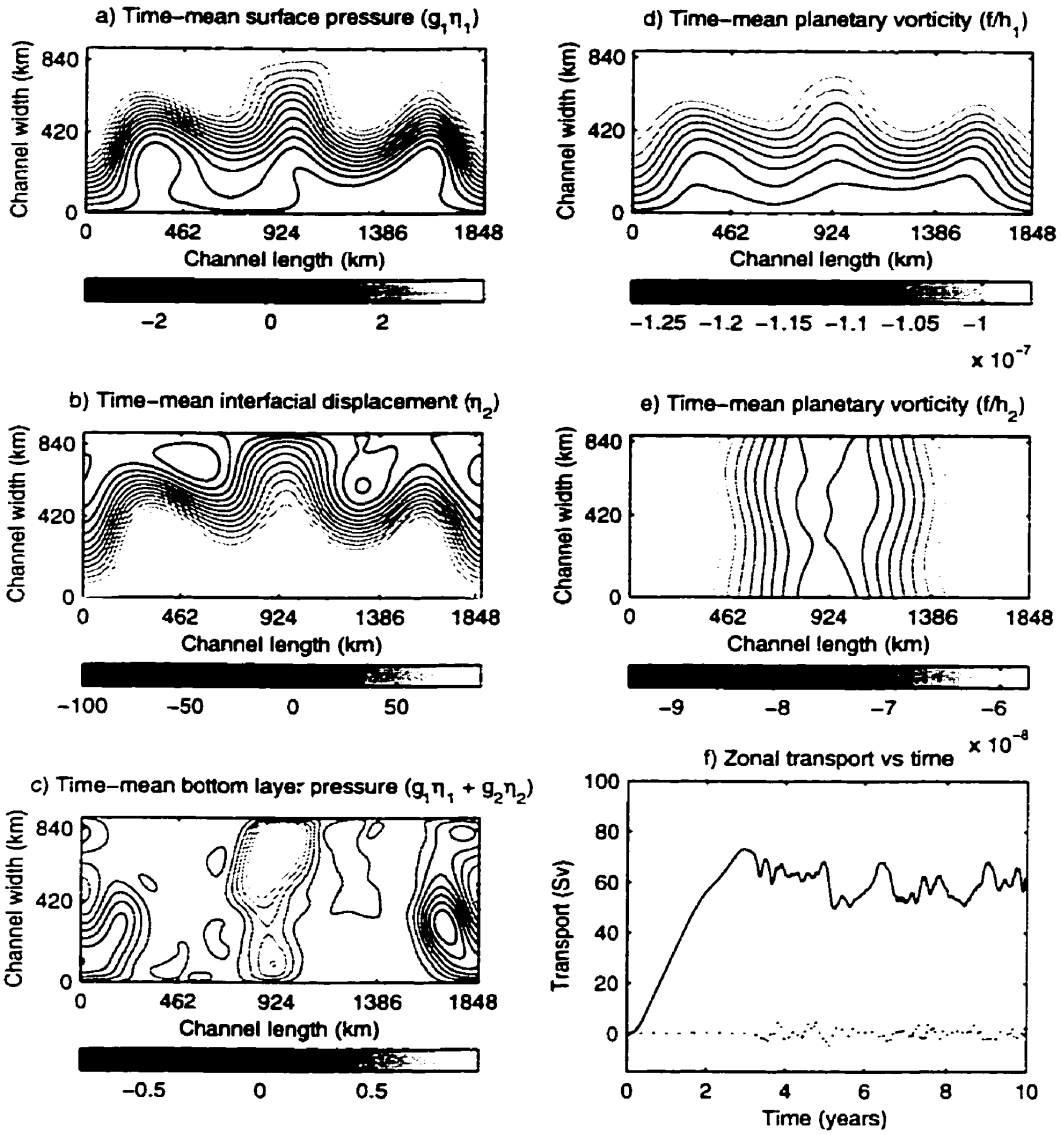

Figure 4.12: Time-mean fields and transport time series for run W2 ($\tau^x = 0.5 \times 10^{-7}$ m s^{-2}). a) Time-mean surface pressure field. Pressures are in m s^{-2}. b) Time-mean bottom pressure field. c) Time-mean interfacial displacement. Height is in meters. d) Time-mean planetary vorticity (f/h_1) in upper layer. e) Time-mean planetary vorticity (f/h_2) in lower layer. f) Zonal transport time series for each layer (Solid line: upper layer, dashed line: lower layer). Shaded scales and number of contours in each panel are the same as in figure 4.1.

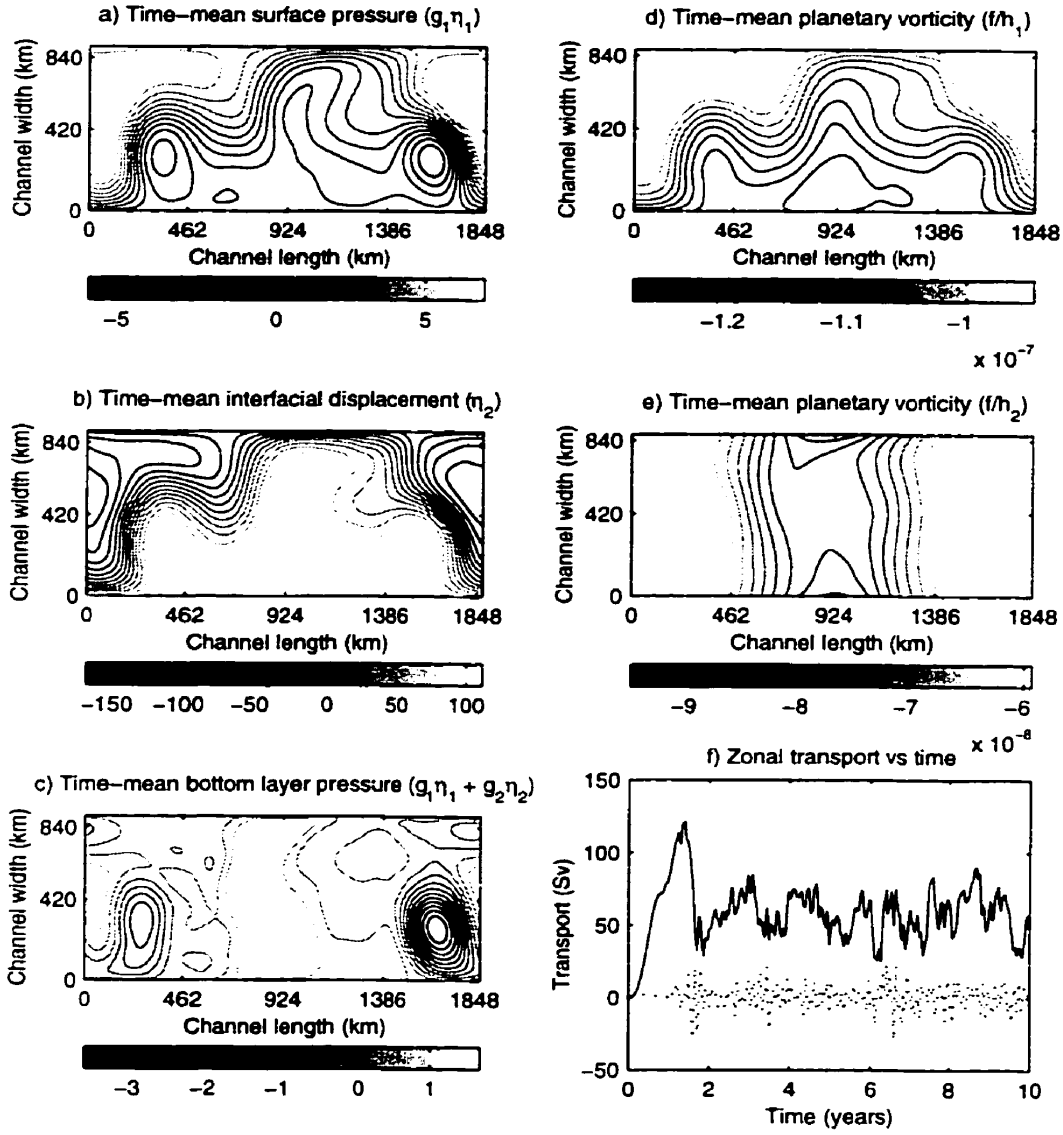

Figure 4.13: Time-mean fields and transport time series for run W4 ($\tau^x = 2.5 \times 10^{-7}$ m s^{-2}). Same as figure 4.12.

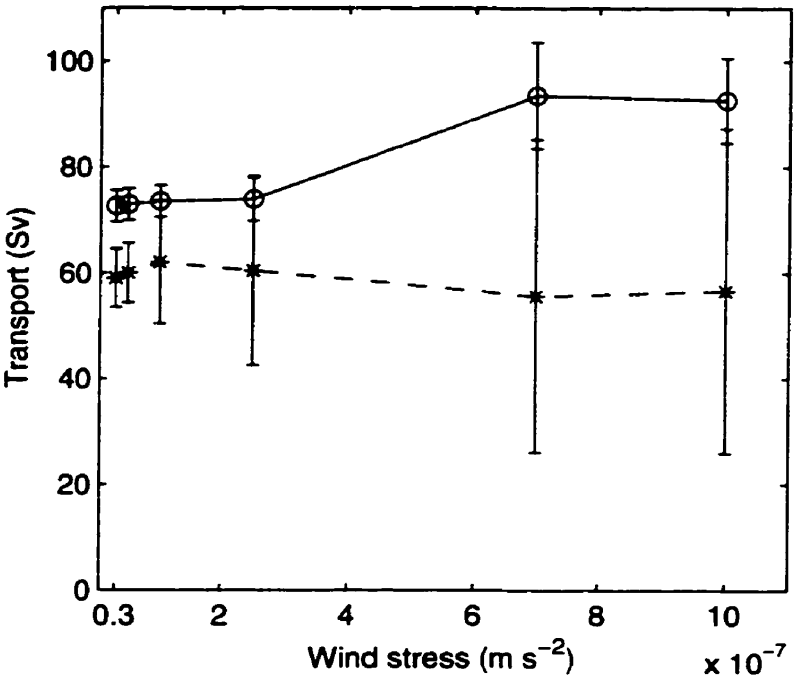

Figure 4.14: Model transports vs applied wind stress. Circles are critical-point transport values and crosses are steady-state transport values.

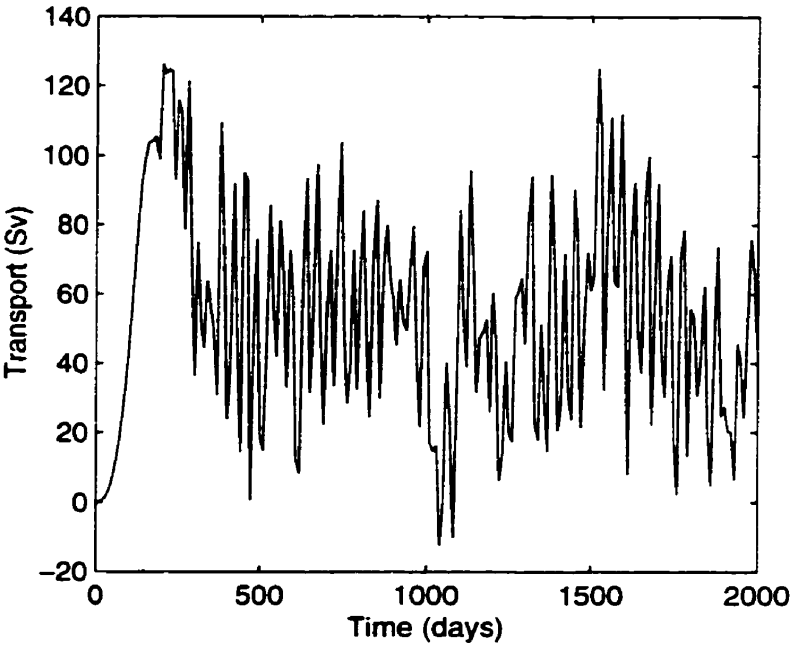

Figure 4.15: Upper-layer transport time series for experiment W6.

4.2.4 Transport dependence on model resolution

The last five model integrations were conducted to test the results' dependence on model resolution. The internal Rossby radius was set to 35 km for all experiments. The five tested models resolution were 12, 14, 21, 24 and 28 km (ref. table 3.4).

Qualitatively, the results are quite similar between experiments at different resolutions. Figures 4.16 and 4.17 show the time-mean flow fields and transport time series for resolutions of, respectively, 12 and 28 km. The surface slope (panel a) is slightly steeper at 12 km but the general features are captured at 28 km. The lower layer circulation presents the most differences. The general locations of the eddies are similar at both resolutions but the eddy strengths are quite different. Also the transport time series exhibit different patterns. The 28-km time series displays a near-yearly cycle which does not appear in the 12-km time series. Instead, the 12-km transport presents more short time scale variability. Smaller eddies are resolved at a 12-km resolution and these are associated with shorter time scales. The coarser 28-km resolution can only capture the larger eddies which take longer to set up and disrupt.

Figure 4.18 presents the model transports obtained for each resolution. The crosses are the critical-point transports and the circles are the steady-state transports. The steady-state transport seems to show a slight increase as the resolution becomes coarser. A variation of about 15% occurs over the investigated range. The critical-point transport remains fairly constant and the variations that can be observed are within the accuracy margin of the measurements. Both transports can be considered to be fairly independent of model resolution.

The transport being independent of model resolution indicates that the linear interpolation for the steady-state transport against the internal Rossby radius should hold as the radius is decreased below 35 km. Recall that for the Rossby radius

experiments, we varied the Rossby radius and kept the resolution constant. To some extent, this provides the same effect as changing the model resolution. A 35 km internal Rossby radius, at 14 km resolution, is less resolved than a 45 km internal Rossby radius at the same resolution. Reducing the Rossby radius is similar to reducing the resolution and as such we can expect the transport to remain linear below 35 km. Consequently, equation 2.10 probably underestimates the transport below 35 km.

This study was undertaken to determine the extent to which the numerical model is solving the analytical equations. We therefore did not vary the Reynolds number in these experiments. A lack of sensitivity of model transport to model resolution implies that we can be confident that our resolution is sufficient for us to draw conclusions about the transport. As an example, the transport time series for runs M1 and M5 exhibit different variability patterns. Obviously, at least one of these two patterns must be slightly unrealistic. Nevertheless, the two patterns both capture the flow characteristics which govern the through-channel transport. Our results show that the resolution we chose was sufficient to study the transport of channel models. We can be confident that these results represent well the analytical solution of the model we studied.

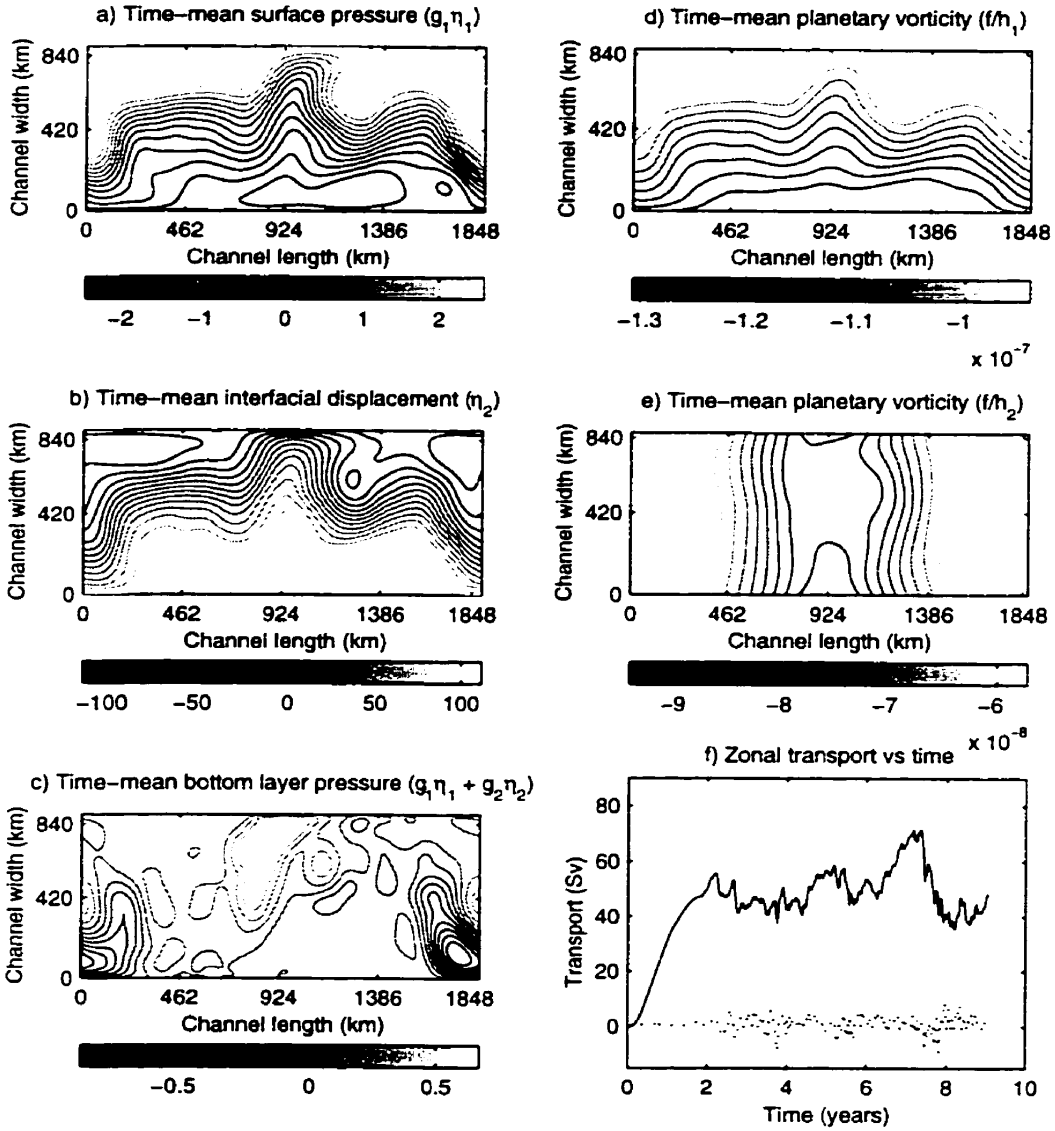

Figure 4.16: Time-mean fields and transport time series for run M1 (12 km resolution). a) Time-mean surface pressure field. Pressures are in m s^{-2}. b) Time-mean bottom pressure field. c) Time-mean interfacial displacement. Height is in meters. d) Time-mean planetary vorticity (f/h_1) in upper layer. e) Time-mean planetary vorticity (f/h_2) in lower layer. f) Zonal transport time series for each layer (Solid line: upper layer, dashed line: lower layer). Shaded scales and number of contours in each panel are the same as in figure 4.1.

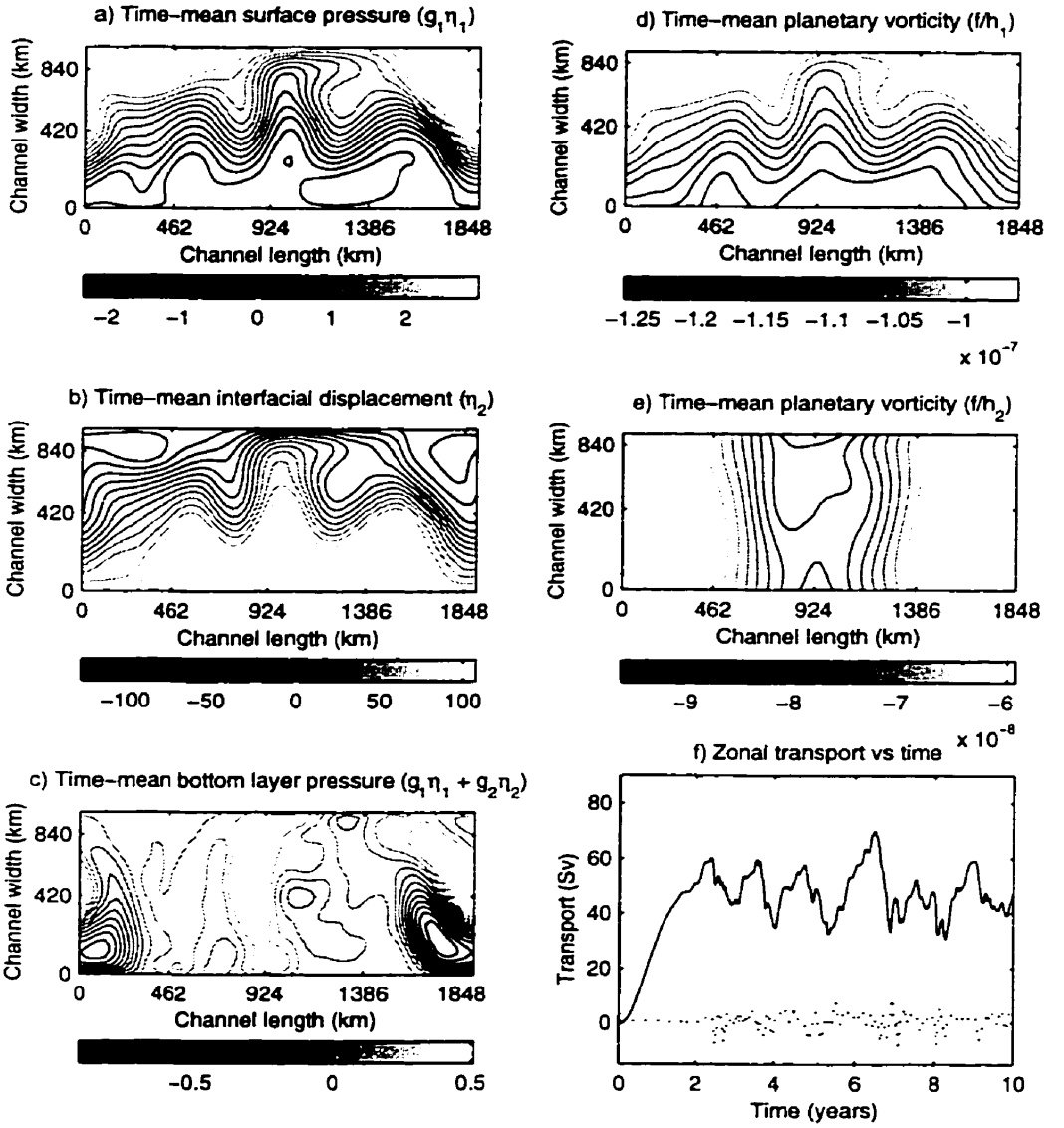

Figure 4.17: Time-mean fields and transport time series for run M5 (28 km resolution). Same as figure 4.16.

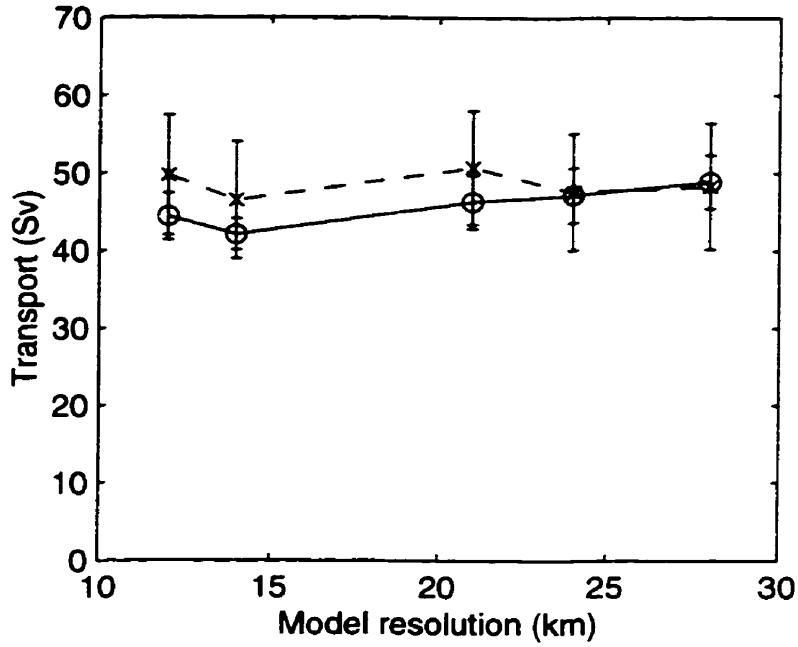

Figure 4.18: Model transports vs model resolution. Crosses are critical-point transport values and circles are steady-state transport values.

Chapter 5

Conclusions

An idealized channel model of the Drake Passage latitude band has been presented. We consider a two-layer ocean with eastward wind forcing. The channel is oriented in the east-west direction and is periodic. The model is characterized by large meridionally-blocking topography contained in the lower layer. The topography is high enough to effectively block geostrophic contours in the lower layer. We therefore have zonally-reconnecting geostrophic contours in the upper layer and blocked contours at depth. The presence of zonally-reconnecting contours in the upper layer inhibits geostrophic meridional flow in the upper layer during model spin-up. To compensate for the equatorward Ekman flux in the upper layer, a geostrophic return flow is therefore required in the lower layer and is supported by topographical form stress and the associated pressure torque. The meridional circulation cannot be closed in each layer individually at this point. Instead, the flow has to become baroclinically unstable to reach a steady-state. Once the flow becomes baroclinically unstable, the movement of the zonally-reconnecting contours, associated with transient eddies, allows for a geostrophic return flow to appear in the upper layer. This return flow is supported by the pressure torque associated with interfacial form drag. The meridional circulation is therefore closed in all layers and the statistical equilibrium can be

attained. From the requirements that the flow become baroclinically unstable and that the through-channel transport be concentrated in the upper layer, we can derive a relationship between the through-channel transport and the internal Rossby radius of deformation, L_R. The transport should be proportional to the square of L_R and also be independent of the wind stress strength.

This relationship was tested using a two-layer primitive-equation channel model. A large meridional ridge was placed in the lower layer to block the geostrophic contours in that layer. The model was forced with a constant wind stress and run for ten years. Statistical equilibrium was generally reached after about four to five model years. The zonal transport rose slowly during model spin-up and exhibited little short time-scale variability. Equilibrium was reached soon after the system became baroclinically unstable. A large portion of the channel became baroclinically unstable at once.

Several model runs were conducted to evaluate the robustness of the predicted relationship between the transport and the Rossby radius. A first series of experiments attempted to identify the dependence of the model transport on the internal Rossby radius of deformation used in the model and compare these results with our theoretical estimate. The internal Rossby radius was varied through changes in the reduced gravity applied to the lower layer. All other parameters were kept constant between each run. Two zonal transport values were defined: the critical point transport value which is taken at the onset of baroclinic instability and the equilibrium value which is a time-mean transport value calculated for the last five model years.

The graph of transport versus internal Rossby radius presents reasonable agreement between theory and experiment. The critical point transport follows a quadratic dependence on the internal Rossby radius as expected by the theory. The transport is a maximum of 11% less than that expected by the theory. The equilibrium transport value exhibits a more linear dependence on the internal Rossby radius. The values

nonetheless decrease with decreasing Rossby radii and remain smaller than the critical point value for most of the range of radii investigated. We conclude that, in the range investigated, the zonal transport in two-layer channel models of the ACC decreases with decreasing Rossby radii and has a value comparable to or smaller than that predicted by the theory.

A second series of experiments was conducted to test robustness to the form and amplitude of the topography. The topographic height and shape were varied separately. The topographic height did not greatly change the flow characteristics and the transport values remained in the same range. A Gaussian-shaped ridge was then tested in place of the usual sinusoidal ridge. The ridge shape significantly affected the flow field. The lower layer display basin-like dynamics as the ridge acted as partial basin walls. However, this different flow configuration did not affect the transport values significantly. All in all, the topographic height and shape only seem important to the extent that they should result in zonally-reconnecting potential vorticity contours in the upper layer and blocked contours at depth. As long as this is respected, the choice of a particular topography should therefore not make any significant impact on the evaluation of our estimate's robustness.

A third series of experiments concentrated on the dependence of model transport to the applied wind stress. Different wind stress strengths were applied but the wind stress shape was maintained constant. No other model parameter was varied between the different runs. The same two transport values were calculated for each run. For a range of applied wind stresses, the model transports remained fairly constant, exhibiting only 10% variance. The critical point transport increased for wind stresses above 5×10^{-7} m s^{-2} although the equilibrium transport remained fairly constant. This is to be expected as the increased wind stress affects the instability process by introducing more inertial (and other) waves which absorb more of the wind-input energy. This energy is therefore not available to force an interfacial slope sufficiently steep to initiate baroclinic instability. It then takes longer for the critical point to be

reached and the associated transport is consequently bigger. We conclude that the zonal transport is fairly independent of the wind stress strength.

The last series of experiments pertained to the dependence of these results on model resolution. Constant internal Rossby radius and wind stress were applied and only the resolution was modified for each run. Both the critical point and equilibrium transports displayed little change (about 10%) with changes in resolution of a factor of two. The steady-state transport exhibited a slight increase as the resolution became coarser while the critical-point transport demonstrated no particular trend. The results were therefore taken to be relatively independent of the model resolution and give confidence in the validity of the transport estimates.

These results validate our estimate of the transport in channel models of the ACC. The through-channel model transport tends to follow the predicted behavior of equation 2.10. We can try and relate this result to the real Southern Ocean. The ACC is influenced by two different contributions: Sverdrup, or basin-like, dynamics which drive the flow from north of Drake Passage and the Drake Passage latitude band dynamics which we tried to understand here. Our results indicate that the non-Sverdrup dynamics south of the ACC need not add significantly to the total ACC transport. The small ($\approx$ 20 km) internal Rossby radius of the Southern Ocean in the Drake Passage latitude band combined to our estimate gives a transport of about only 20 Sv. When added to the Sverdrup-dynamics Drake Passage transport of about 120 Sv to 160 Sv (*e.g.*, Baker, 1982, Chelton *et al.* , 1990, Warren *et al.* , 1996), the total transport remains close to the measured ACC transport of 130 Sv.

The model's requirement of baroclinic instability is supported by other model results. Cane and Krupitsky (1997) suggest that our mechanism is easily applicable to the Southern Ocean. Many other model analyses (*e.g.*, Ivchenko *et al.* , 1997, Gille, 1997) have demonstrated the presence of transient eddies in the Drake Passage latitude band as our model suggests.

It is important to remember that our model does not attempt to reproduce ACC dynamics perfectly. Rather, we concentrated on only half of the problem. and tried to shed some light on the particular dynamics of the only zonally-unbounded region of the Earth.

Bibliography

BAKER, J. D. (1982). A note on Sverdrup balance in the Southern Ocean. *Journal of Marine Research*, 40 (Suppl.):21–26.

BRYDEN, H. L. AND HEATH, R. A. (1985). Energetic eddies at the northern edge of the Antarctic Circumpolar Current. *Progress in Oceanography*, 14:65–87.

CHELTON, D. B., MESTAS-NUNEZ, A. M., AND FREILICH, M. (1990). Global wind stress and Sverdrup circulation from the Seasat scatterometer. *J. Phys. Oceanogr.*, 20:1175–1205.

DÖÖS, K. AND WEBB, D. J. (1994). The Deacon cell and other meridional cells of the Southern Ocean. *J. Phys. Oceanogr.*, 24:429–442.

FRAM GROUP (1991). An eddy-resolving model of the Southern Ocean. *EOS. Trans. Americ. Geophys. Union*, 72:169–175.

GILL, A. E. AND BRYAN, K. (1971). Effects of geometry on the circulation of a three-dimensional southern-hemisphere ocean model. *Deep Sea Research*, 18:685–721.

GILL, A. (1968). A linear model of the Antarctic Circumpolar Current. *Journal of Fluid Mechanics*, 32:465–488.

GILLE, S. T. (1997). The Southern Ocean momentum balance: Evidence for topographic effects from numerical output and altimeter data. *J. Phys. Oceanogr.*, 27:2219–2232.

GODFREY, J. S. (1989). A Sverdrup model of the depth-integrated flow for the world allowing for island circulations. *Geophys. Astrophys. Fluid Dyn.*, 45:89–112.

HELLERMAN, S. AND ROSENSTEIN, M. (1983). Normal monthly wind stress over the world ocean with error estimates. *J. Phys. Oceanogr.*, 13:1093–1104.

HIDAKA, K. AND TSUCHIYA, M. (1953). On the Antarctic Circumpolar Current. *Journal of Marine Research*, 12:214–222.

HOURY, S., DOMBROWSKI, E., DE MEY, P., AND MINSTER, J.-F. (1987). Brunt-Väisälä frequency and Rossby radii in the South Atlantic. *J. Phys. Oceanogr.*, 17:1619–1626.

HUGHES, C. W. (1997). Comments on "On the obscurantist physics of 'form drag' in theorizing about the Circumpolar Current". *J. Phys. Oceanogr.*, 27:209–210.

ISHIDA, A. (1994). Effects of partial meridional barriers on the Antarctic Circumpolar Current - Wind-driven barotropic model. *Dyn. Atmos. Oceans*, 20:315–341.

IVCHENKO, V. O., RICHARDS, K. J., AND STEVENS, D. P. (1996). The dynamics of the Antarctic Circumpolar Current. *J. Phys. Oceanogr.*, 26:753–774.

IVCHENKO, V. O., TREGUIER, A. M., AND BEST, S. E. (1997). A kinetic energy budget and internal instabilities in the Fine Resolution Antarctic Model. *J. Phys. Oceanogr.*, 27:5–22.

JOHNSON, G. C. AND BRYDEN, H. L. (1989). On the size of the Antarctic Circumpolar Current. *Deep Sea Research*, 36(1):39–53.

KILLWORTH, P. D. (1995). An equivalent barotropic mode in the Fine Resolution Antarctic Model. *J. Phys. Oceanogr.*, 22:1379–1387.

KRUPITSKY, A. AND CANE, M. A. (1997). A two-layer wind-driven ocean model in a multiply connected domain with bottom topography. *J. Phys. Oceanogr.*, 27:2395–2404.

KRUPITSKY, A., KAMENKOVICH, V. M., NAIK, N., AND CANE, M. A. (1996). A linear equivalent barotropic model of the Antarctic Circumpolar Current with realistic coastlines and bottom topography. *J. Phys. Oceanogr.*, 26:1803–1824.

LEVITUS, S. (1982). Climatological Atlas of the World Ocean. Report, NOAA Prof. Pap. 13, US Government Printing Office, Washington, DC.

MARSHALL, D. (1995). Topographic steering of the Antarctic Circumpolar Current. *J. Phys. Oceanogr.*, 25:1636–1650.

MARSHALL, D., OLBERS, D. J., ROSS, H., AND WOLF-GLADROW, D. (1993). Potential vorticity constraints on the dynamics and hydrography of the Southern Ocean. *J. Phys. Oceanogr.*, 23:465–487.

MCWILLIAMS, J. C., HOLLAND, W. R., AND CHOW, J. H. S. (1978). A description of numerical Antarctic Circumpolar Currents. *Dyn. Atmos. Oceans*, 2:213–291.

MEREDITH, M. P., VASSIC, J. M., HEYWOOD, K. J., AND SPENCER, R. (1996). On the temporal variabilty of the transport through Drake Passage. *J. Geophys. Res.*, 101:22485–22494.

MUNK, W. H. AND PALMEN, E. (1951). Note on the dynamics of the Antarctic Circumpolar Current. *Tellus*, 3:53–55.

NOWLIN, W. D. JR AND KLINCK, J. M. (1986). The physics of the Antarctic Circumpolar Current. *Rev. Geophys.*, 24:788–802.

NOWLIN, W. D. JR, WHITWORTH, T. I., AND PILLSBURY, R. D. (1977). Structure and transport of the Antarctic Circumpolar Current at Drake Passage from short-term measurements. *J. Phys. Oceanogr.*, 7:788–802.

OLBERS, D. J. AND WENZEL, M. (1989). Determining diffusivities from hydrographic data by inverse methods with applications to the circumpolar current. In WILLEBRAND, J. AND ANDERSON, D. L. T., editors, *Modelling the Ocean General Circulation and Geochemical Tracer Transport*, NATO ASI Series C, pages 95–122. Kluwer Academics.

RICHTMYER, R. D. (1967). *Difference Methods for Initial-Value-Problems.* Interscience, 2nd edition.

SEMTNER, A. J. AND CHERVIN, R. M. (1992). Ocean general circulation from a global eddy-resolving model. *J. Geophys. Res.*, 97:5493–5550.

STOMMEL, H. (1957). A survey of ocean current theory. *Deep Sea Research*, 4:149–184.

STOMMEL, H. (1962). An analogy to the Antarctic Circumpolar Current. *Journal of Marine Research*, 20:92–96.

STRAUB, D. N. (1993). On the transport and angular momentum balance in channel models of the Antarctic Circumpolar Current. *J. Phys. Oceanogr.*, 23:776–782.

TOGGWEILER, J. R. AND SAMUELS, B. (1995). Effect of Drake Passage on the global thermohaline circulation. *Deep-Sea Research. Part I: Oceanographic Research Papers*, 42:477–500.

TOGGWEILER, J. R. AND SAMUELS, B. (1998). On the ocean's large-scale circulation near the limit of no vertical mixing. *J. Phys. Oceanogr.*, 28:1832–1852.

TREGUIER, A. M. AND MCWILLIAMS, J. C. (1990). Topographic influences on wind-driven, stratified flow in a β-plane channel: An idealized model for the Antarctic Circumpolar Current. *J. Phys. Oceanogr.*, 20:321–343.

WARREN, B. A., LACASCE, J. H., AND ROBBINS, P. E. (1996). On the obscurantist physics of "form drag" in theorizing about the Circumpolar Current. *J. Phys. Oceanogr.*, 26:2297–2301.

WARREN, B. A., LACASCE, J. H., AND ROBBINS, P. E. (1997). Reply. *J. Phys. Oceanogr.*, 27:211–212.

WEARN, R. B. J. AND BAKER, D. J. J. (1980). Bottom pressure measurements across the Antarctic Circumpolar Current and their relation to wind. *Deep Sea Research*, 27:875–888.

WHITWORTH, T, III (1988). The Antarctic Circumpolar Current. *Oceanus*, 31:53–58.

WHITWORTH, T. III, NOWLIN, W. D. JR, AND WORLEY, S. (1982). The net transport of the Antarctic Circumpolar Current through Drake Passage. *J. Phys. Oceanogr.*, 12:960–971.

WHITWORTH, T. III AND PETERSON, R. G. (1985). The volume transport of the Antarctic Circumpolar Current from bottom pressure measurements. *J. Phys. Oceanogr.*, 15:810–816.

WOCE D.I.U. (1998). WOCE data set, version 1. CD-ROM.

WOLFF, J.-O., MAIER-REIMER, E., AND OLBERS, D. J. (1991). Wind-driven flow over topography in a zonal β-plane channel: A quasi-geostrophic model of the Antarctic Circumpolar Current. *J. Phys. Oceanogr.*, 21:236–264.